

4

Flood Mapping Using Synthetic Aperture Radar Sensors From Local to Global Scales

Antara Dasgupta^{1,2,3}, Stefania Grimaldi³, RAAJ Ramsankaran², Valentijn R. N. Pauwels³,
Jeffrey P. Walker³, Marco Chini⁴, Renaud Hostache⁴, and Patrick Matgen⁴

ABSTRACT

Synthetic aperture radar (SAR) sensors have emerged as the preferred mode of flood monitoring due to their all-weather, all-day imaging capabilities. Current and upcoming SAR satellites provide high-resolutions and shorter revisit times, which can facilitate effective resource allocation during emergency response. However, the sensitivity of microwaves to surface roughness and the side-looking imaging geometry often result in ambiguity in flood detection. This chapter provides an overview of the challenges and opportunities associated with operational SAR-based flood mapping at multiple scales. The principles of SAR imaging are outlined with reference to flood detection problems, and the state-of-the-art solutions proposed in literature to eliminate these effects are critically discussed. Finally, a few selected case studies that demonstrate the potential of SAR-derived extents for operational flood mapping are presented.

4.1. INTRODUCTION

Flooding involves large inundated regions, which are often inaccessible or ungauged. Remote sensing (RS) data provide an elegant and practicable solution to assess spatiotemporal flood evolution. RS-based flood mapping has witnessed significant research breakthroughs over the last decade. In addition to providing stakeholders with timely and spatially distributed information for crisis response [Schumann *et al.*, 2016], RS-based flood maps are now utilized for hydrodynamic model calibra-

tion and evaluation and to improve forecasts through assimilation [Schumann and Domeneghetti, 2016].

The cost of high resolution (>4 and ≤ 10 m) imagery and sparse temporal coverage previously acted as a deterrent to unlocking the full potential of RS for flood management. In 1999, the International Charter “Space and Major Disasters” was initiated to provide a unified system of rapid satellite data acquisition and delivery in the face of major disasters [Martinis *et al.*, 2015b]. Floods are so frequently occurring and globally pervasive, that more than 50% of all satellite data requests through the charter were flood related in the past decade, as illustrated in Figure 4.1. The launch of several high-resolution SAR missions has also contributed to improvements in the spatial and temporal resolutions and global coverage, making their use in flood mapping more practical. A summary of currently operational, historical, and planned SAR missions is presented in Figure 4.2, with Table 4.1 providing details of the sensor characteristics.

Sensors operating in the visible region of the electromagnetic (EM) spectrum offer the most straightforward

¹IITB-Monash Research Academy, Mumbai, Maharashtra, India

²Hydro-Remote Sensing Applications (H-RSA) Group, Department of Civil Engineering, Indian Institute of Technology Bombay, Mumbai, Maharashtra, India

³Water Group, Department of Civil Engineering, Monash University, Melbourne, Victoria, Australia

⁴Department of Environmental Research and Innovation, Luxembourg Institute of Science and Technology, Belvaux, Esch-sur-Alzette, Luxembourg

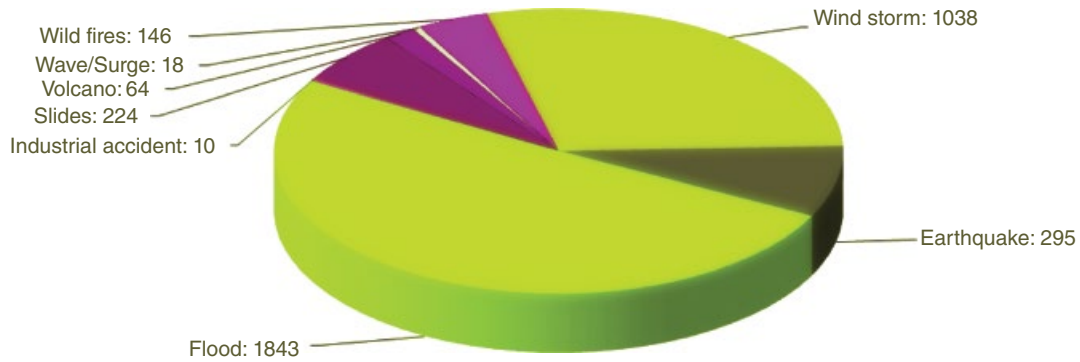


Figure 4.1 Distribution of hazard types for Charter activations between 2000 and 2010. From EM-DAT: The OFDA/CRED International Disaster Database (www.emdat.be – Université catholique de Louvain, Brussels, Belgium).

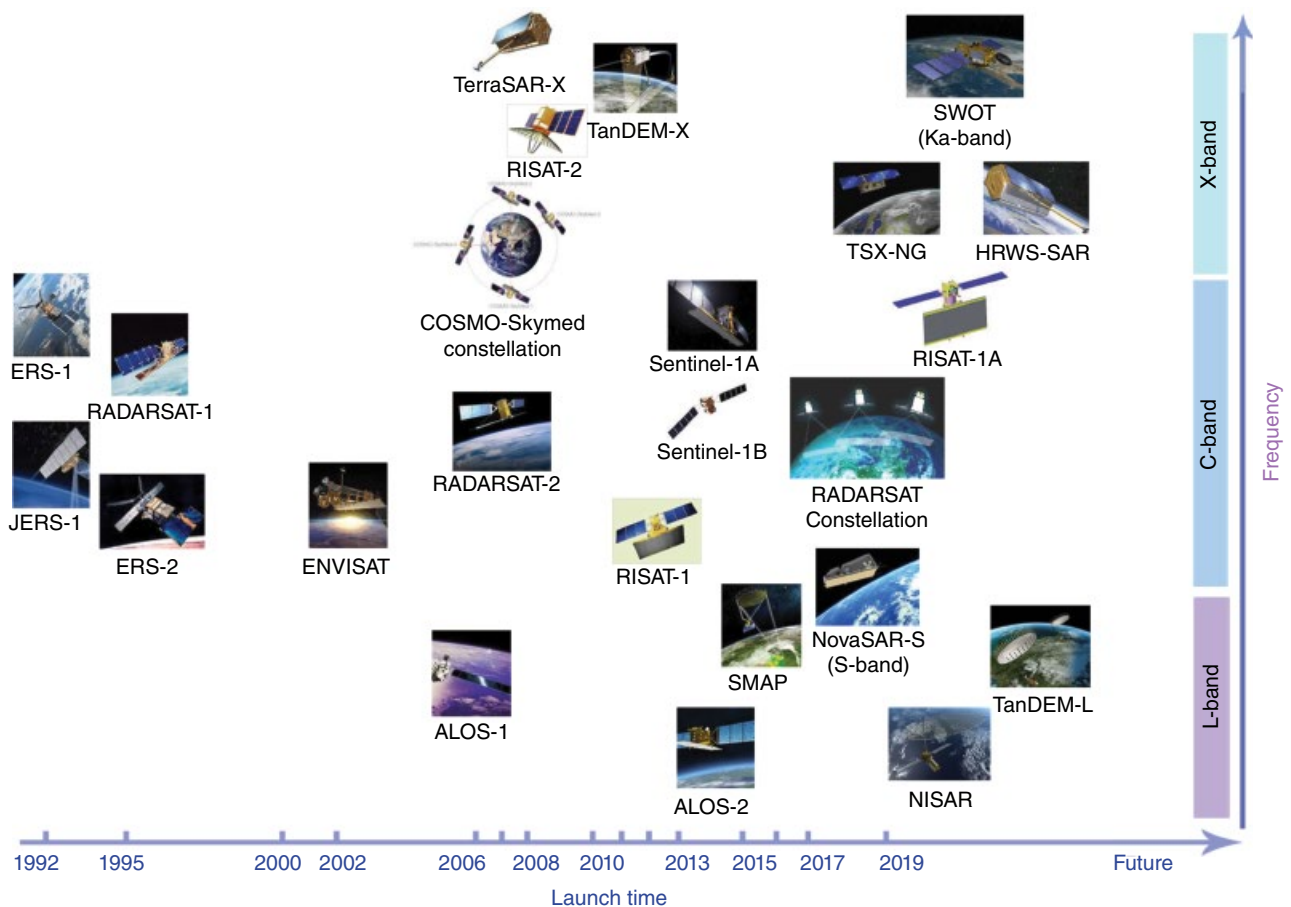


Figure 4.2 Summary of satellite-based SAR missions that are applicable for flood studies, with corresponding wavelength bands and frequencies illustrated.

solution for flood monitoring. Optical RS data are easy to interpret and multiple studies have demonstrated the utility of optical RS for flood mapping [Ordoyne and Friedl, 2008; Li et al., 2015; Blasco et al., 1992; Ogilvie et al., 2015; Jain et al., 2005]. The increasing number of optical sensors with comparatively shorter revisit times, has improved the spatiotemporal coverage substantially.

However, as flood events are frequently characterized by persistent cloud cover, systematic monitoring using optical sensors is challenging.

Microwave remote sensing in the longer wavelength regions is able to penetrate clouds, which obstruct the view of optical sensors. Synthetic Aperture Radar (SAR) sensors use active imaging techniques and therefore can

Table 4.1 Summary of Spaceborne SAR Missions and Sensor Characteristics

SAR Platform	Band	Polarization	Look angle (°)	Swath (km)	Resolution (m)	Repeat cycle (days)	Mission status
ALMAZ-1	S	Single	20–70	350	10–30		Completed
ALOS PALSAR-1	L	Dual	10–51	40–350	6.25–100	46	Completed
ALOS PALSAR-2	L	Quad	8–70	25–350	1–100	14	Active
<i>COSMO-SkyMED (CSK)</i>	<i>X</i>	<i>Quad</i>	<i>20–59.5</i>	<i>10–200</i>	<i>1–100</i>	<i><1</i>	<i>Active</i>
<i>CSK-2</i>	<i>X</i>	<i>Quad</i>	<i>–</i>	<i>40–200</i>	<i>0.8–20</i>	<i>–</i>	<i>Planned</i>
Envisat ASAR	C	Quad	14–45	58–405	30–1000	35	Completed
ERS-1/2 AMI	C	Single	23	100	30	35	Completed
JERS-1	C	Single	35	75	18	44	Completed
KOMPSAT-5	X	Quad	20–55	5–100	1–20	28	Active
NISAR	L, S	Quad	–	–	–	–	Planned
NovaSAR-S	S	Dual	–	15–150	6–30	–	Planned
RADARSAT-1	C	Single	10–60	45–500	8–100	24	Completed
RADARSAT-2	C	Quad	10–60	10–500	3–100	24	Active
<i>RCM</i>	<i>C</i>	<i>Quad</i>	<i>–</i>	<i>20–350</i>	<i>5–50</i>	<i>1–4</i>	<i>Planned</i>
RISAT-1	C	Quad	12–55	10–225	1–50	4	Active
RISAT-2	X	Quad	20–45	10–50	1–8	4	Active
RISAT-1A	C	Quad	12–55	10–225	1–50	4	Planned
SEASAT-1	L	Single	20–26	100	25	17	Completed
Sentinel-1A/B	C	Quad	20–45	20–400	5–100	6	Active
SIR-A	L	Single	47–53	40	40	–	Completed
SIR-B	L	Single	15–60	10–60	15–45	–	Completed
SIR-C	X, C, L	Quad	15–60	15–90	15–45	–	Completed
TerraSAR/ TanDEM-X	X	Quad	15–60	5–200	0.24–40	11	Active
TanDEM-L	L	Quad	–	~350	1–20	16	Planned
TSX-NG	X	Quad	20–55	5–400	1–30	–	Planned
TerraSAR-X (HRWS-SAR)	X	Quad	–	10–800	0.25–25	–	Planned

Note: The italicized entries indicate satellite constellations with identical configurations.

Source: Modified based on Lillesand et al. [2004].

function independent of solar illumination or weather conditions. This property is indispensable for small to medium sized catchments, where flood waters often retreat before the cloud cover dissipates sufficiently [Schumann et al., 2007a]. Consequently SAR data are currently the only reliable source of information for monitoring riverine floods for small catchments with subkilometer channel widths [Schumann and Moller, 2015].

Similar to the response of a mirror, a smooth surface, or what is often referred to as a specular reflector in microwave remote sensing, reflects the radar beam back at an angle equal and opposite to the angle of incidence. This causes smooth or level surfaces to appear black in SAR images as the radar return is not recorded by the antenna. Conversely, land surfaces with multiple objects appear rough to the sensor and return high backscatter. It is this high contrast in backscatter values recorded for land and water that facilitates surface water detection in SAR imagery.

Flood extent information can facilitate not only effective regional prioritization, but also efficient resource

allocation, both during and after events. For ungauged catchments and inaccessible regions, SAR-based flood maps are frequently used in combination with high resolution topographic data to derive spatially distributed water levels [Barreto et al., 2016; Frappart et al., 2006; Hostache et al., 2009; Schumann et al., 2007; Matgen et al., 2016]. SAR-derived water levels (WL) are often used as hydrodynamic model calibration and validation targets [Pappenberger et al., 2007; Schumann et al., 2008a; Di Baldassarre et al., 2009; Gobeyn et al., 2015, 2017; Gupta et al., 1998; Horritt, 2000; Horritt and Bates, 2002; Hostache et al., 2006; Wood et al., 2016], or assimilated into the model trajectory for an improved forecasting skill [García-Pintado et al., 2013; García-pintado et al., 2014; Hostache et al., 2010; Lai and Monnier, 2009; Mason et al., 2012a; Matgen et al., 2010].

The last few years have seen a massive increase in utilization of spaceborne SAR systems for flood extent mapping, as new high-resolution platforms like TerraSAR-X/TanDEM-X and the COSMO-SkyMed constellation became operational, as shown in Figure 4.2 [Martinis and

Rieke, 2015; Pradhan *et al.*, 2016, 2014; Voormansik *et al.*, 2014; Pierdicca *et al.*, 2014; Pierdicca *et al.*, 2013; Pulvirenti *et al.*, 2011a and b, 2012, 2013, 2014a and b]. Launch of the Sentinel-1A/B twin satellites, which provide global SAR coverage at 20 m spatial resolution with a revisit time of 3 days (and a repeat cycle of 6), marks a shift toward open data sharing in the satellite industry. Moreover, accessibility to fine resolution SAR imagery has already triggered a plethora of automated flood extraction algorithms [Boni *et al.*, 2016; Sala *et al.*, 2016; Twele *et al.*, 2016]. It can therefore be envisioned that the next decade will witness an inclusive data sharing environment conducive to operational SAR-based flood mapping.

As operational flood mapping needs to facilitate rapid image interpretation, low-resolution datasets can be used to assess flood hazards at global scales [Westerhoff *et al.*, 2013; Giustarini *et al.*, 2015b]. This diagnostic analysis can be utilized to identify areas of high hydraulic complexity, where finer scale imagery needs to be used. Such analysis can potentially inform variable resolution global flood models, which can be used to optimize the utilization of computational resources [Mason *et al.*, 2015]. As high-resolution image processing as well as modeling are associated with significant computational costs, it's vital to utilize data at scales appropriate for the flood event under investigation.

This chapter provides a discussion on the issues related to operational SAR-based flood mapping at multiple scales and current progress in finding practicable solutions. First, the characteristics of SAR signals and surface feature interactions are discussed along with their implications for flood mapping and proposed solutions in literature. This is followed by an overview of the state of the art in SAR-based flood delineation techniques. Furthermore, some selected case studies from recent literature, which demonstrate the potential of SAR-derived extents for flood studies at different spatial scales, are given. Finally, future work and open research questions in SAR-based flood mapping have been elucidated.

4.2. PRINCIPLES OF SAR: IMPLICATIONS FOR FLOOD MAPPING

Microwave interactions with the Earth's surface are governed by the SAR sensor configuration (wavelength, polarization, resolution, and looking angle), surface characteristics (roughness and dielectric properties), and local slope. The high contrast in the radar image between flooded and nonflooded areas is primarily the result of specular reflection from standing water. This phenomenon makes water surfaces appear dark on SAR images, as opposed to the increased scattering from rough land surfaces, which makes terrain appear bright. As floods are mainly identified using the changes they cause in

backscattering behavior of land cover classes, flood mapping is then detecting the insurgence of water in three main land cover classes: bare soil, vegetation, and urban areas. In order to understand these changes, one needs to be aware of the underlying mechanisms that drive the microwave interactions with the Earth's surface.

4.2.1. Geometric Distortion

The SAR side-looking sensing implies that two points will look closer in the slant-range image than they actually are on the ground. This effect gets more pronounced as we move closer to the antenna (i.e., in the near range) and is most noticeable at nadir (90°). The projection lines from the ground-range to slant-range are usually in the form of concentric circles around the antenna, due to the spherical divergence of radar pulses over such large distances. This leads to geometric distortion in the images, which needs to be accounted for in flood mapping problems.

The imaging of steep vertical objects through SAR results in a phenomenon known as relief displacement. The top of the structure shifts from its actual ground location, proportional to object height and radar look angles. In particular, these errors can be of three types:

1. *Foreshortening*: As radar imaging records distances from the antenna, the top of tall targets such as mountains would be encountered by the beam before the bottom is seen. This makes the object appear to “lean” toward the sensors with the foreslope (the slope facing the sensor) appearing shorter than in reality.

2. *Layover*: When slopes are steeper, targets in the valley region behind the mountains display a longer slant range. This causes objects in the slant range to be ordered in reverse of their actual ground positioning. Consequently, the front slope appears to overlay on the backslope on the SAR image.

3. *Shadow*: This effect is caused primarily by the side-looking imaging technique. As the radar views objects at an angle, it cannot “see” a certain region hidden by vertical structures, these appear as dark shadows in the SAR image.

4.2.2. Surface Roughness and Local Incidence Angle

Radar backscatter is a function of the surface roughness and local incidence angle of the surface from which the radar beam is scattered. See Figure 4.3. The nature of this scattering determines the strength of the signal returned to the sensor and can be of the following types.

4.2.2.1. Surface Scattering

The scale of the surface roughness can be represented by the root-mean-square deviation (h) from the mean

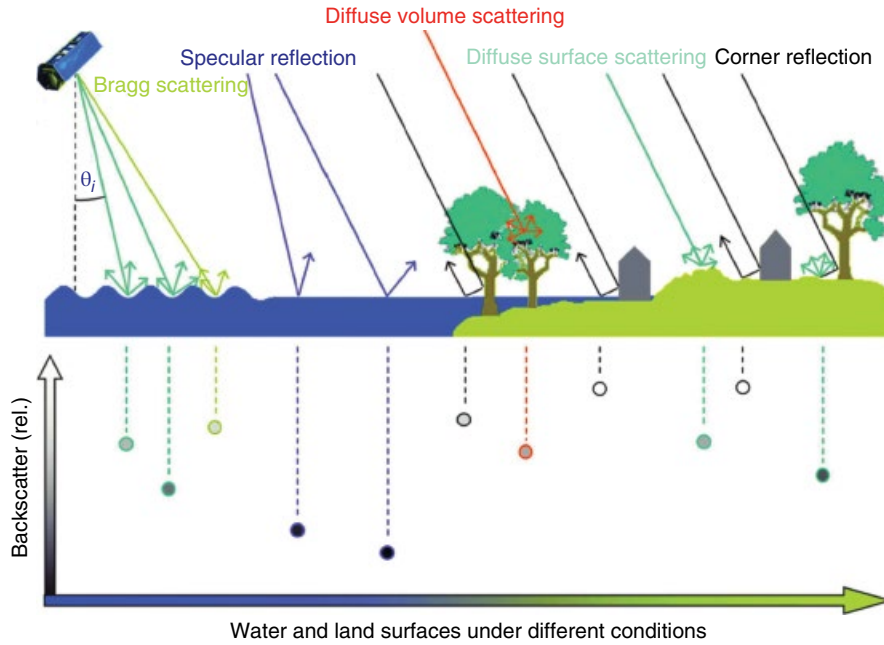


Figure 4.3 Different scattering mechanisms displayed by radar interactions with water and land surfaces. Based on Martinis et al. [2015].

height (\bar{h}) of the interface dividing the two homogeneous media, the atmosphere, and the hypothetical perfectly smooth open water surface. Intuitively, one can imagine that when this deviation is comparable to the magnitude of the wavelength, the surface undulations return separate radar echoes to the antenna. The interference of these returned signals spuriously raises the recorded backscatter values, leading to a reduction in specular reflection effects.

According to the Rayleigh criterion, the phase change caused by h should be less than a quarter of the wavelength (λ). As this phase difference increases, scattering becomes more diffuse (i.e., energy is reflected equally in all directions) and “smooth” surfaces are no longer detectable by the contrast. The local incidence angle, θ_{loc} , determines the path difference between the incident and the scattered path, and therefore can influence the maximum acceptable value of h for smooth surfaces. The Rayleigh criterion describes smooth surfaces as those satisfying

$$h < \frac{\lambda}{8 \cos \theta_{loc}} \quad (4.1)$$

Equation 4.1 implies that h must be 1/8 of the wavelength to account for two-way travel of the radar path. In case of RS, a stricter criterion for smoothness is needed, known as the Fraunhofer criterion, which restricts h to 1/32 of λ , as the distance between the target and the sensor is usually several orders of magnitude larger than the wavelength of the incident beam. Based on the above,

surface scattering mechanisms can broadly be classified into two categories:

1. *Specular scattering (or reflection)*: Where the majority of the incident microwave energy is reflected off a smooth surface; the remaining energy is transmitted through the media in accordance with Snell law of refraction. Radar returns are negligible for a perfect specular reflector as the beam is reflected away from the receiver.

2. *Bragg scattering*: When the surface roughness of a slightly rough $\left(\frac{\lambda}{32} < h < \frac{\lambda}{8}\right)$ homogeneous medium exhibits periodicity, an identifiable and coherent pattern of backscatter is returned. Bragg surfaces are often an ordered collection of facets, where particular orientations occur at regular intervals. The facets oriented toward the sensor can often produce return signals, which resonate with the incident beam resulting in bright image regions. This effect is more pronounced for steeper incidence angles as the sensor may record backscatter returned from both specular and Bragg scattering.

3. *Diffuse surface scattering*: As the surface roughness increases beyond 1/8 of the wavelength, the scattering gets more random. An extremely rough surface should ideally scatter the radar beam in all directions with equal intensities, resulting in higher signal returns.

4. *Corner reflection*: The radar pulse is reflected back to the sensor when it encounters a smooth horizontal and smooth vertical surface orthogonal to each other, resulting in saturated pixels. Corner reflection can be caused by partially submerged vegetation or urban

features such as roads, pavements, and buildings, resulting in very strong returns.

4.2.2.2. Volume Scattering

Radar beams achieve measurable penetration depths directly proportional to the incident wavelength. Complex natural environments often include multiple media, having different dielectric constants, which results in volume scattering. When microwaves come in contact with a heterogeneous media exhibiting variations in electromagnetic properties, each wave is scattered in many different directions. The intensity of returned backscatter is a function of the density and heterogeneity of the traversed media. The shape, density, relative permittivity, and orientations of the various media encountered by the radar signal then determine the strength of the backscatter recorded at the antenna.

4.2.3. Dielectric Constant

The dielectric constant is defined as the ratio between the electrical permittivity of a homogeneous material with respect to that of vacuum, given by a dimensionless quantity also known as relative permittivity. Natural materials do not respond to external electromagnetic fields instantaneously, unlike vacuum. The response generally depends on the frequency of the applied field, which in this case is the radar signal.

Microwave frequencies are highly sensitive to changes in the dielectric constant, and can achieve considerable penetration depths as most dry natural materials exhibit values between 3 and 8, resulting in low reflectivity in this region of the EM spectrum. Conversely, liquid water has a dielectric constant of approximately 80 in the microwave region. Based on this, open water should return most of the signal right back to the sensor, exhibiting strong reflectivity. This doesn't happen in reality as the effects of specular reflection dominate and the beam is directed away from the sensor.

Since the dielectric constant is directly correlated to the moisture content per unit volume, higher vegetation/soil water content implies larger values of radar returns. Most of the sensible variation in backscatter recorded from natural surfaces can be explained by the moisture content of the underlying geographical features. This property is often exploited in the derivation of remote sensing based soil moisture. As the dielectric constant depends on the frequency of the EM wave, the penetration depth is directly related to the wavelength. For instance, when detecting flooding under forests, using a SAR image operating in the longer wavelength region (lower frequency) allows the EM waves to penetrate the canopy to a greater extent than shorter wavelengths, which experience surface scattering.

4.2.4. Polarization

The polarization of a SAR image refers to the orientation of the electric field intensity vector in the transmitted and received radar waveform. SAR sensors usually send and receive horizontally polarized waves, as the returns recorded are higher than in vertical polarization. When the transmitted and received radar wave polarizations are identical this is known as copolarized; conversely cross-polarization refers to opposite send and receive polarizations. Fully polarimetric SAR images (antenna can record HH, HV, VH, and VV returns simultaneously) can be useful for detecting flooding under vegetation or urban areas as illustrated in the following sections because they are able to highlight the double-bounce component of the surface scattering.

4.2.5. Speckle

SAR images are affected by conspicuous bright and dark spots known as shot noise or speckle. This apparently random manifestation of light and dark pixels arises from constructive and destructive interference of scattered radar waves. A SAR pixel represents a few square meters of area on the ground, often presenting the incident microwaves with multiple scatterers. These waves, which are scattered nonuniformly in all directions, interfere with one another before reaching the antenna. If this interference is constructive (the crests and troughs of the waveform superimpose), a strong signal return is recorded leading to a bright spot in the SAR image; conversely destructive interference causes the dark spots.

Speckle can be modeled as a random noise effect and several filtering techniques have been proposed to deal with this particular phenomenon over the years. Research suggests that the choice of the particular filtering technique chosen should be governed by the final application. Lee, Frost, Enhanced Lee, median, and Gamma-Maximum-A-Posteriori are some of the speckle filters commonly applied as preprocessors to SAR-based flood detection studies [Voormansik *et al.*, 2014; Martinis *et al.*, 2009]. For additional reading, see Ulaby *et al.* [2014], Rees [2013], and Woodhouse [2005].

4.3. COMMON SAR-BASED FLOOD MAPPING METHODS

A large variety of methods have been introduced in the recent past to map water bodies using SAR imagery. When favorable conditions prevail, a single SAR image acquired during a flood (hereafter referred to as “flood image”) can be sufficient to reliably detect terrestrial water bodies. The single image technique works best when there is no wind roughening the water surface and

when the detection is limited to floodwaters on bare soils and scarcely vegetated terrains. However, it is widely recognized that it is preferable to consider at least a pair of images consisting of the flood image and an adequate reference image (i.e., an image acquired in nonflooded conditions) as change detection not only tends to improve the classification accuracy, but also helps to distinguishing permanent and transient water bodies [Chini *et al.*, 2017]. Eventually, only an approach taking advantage of a dense time series of backscatter recordings derived from tens or hundreds of SAR images acquired over a given area provides all the information that is needed to fully understand a floodplain's backscatter response to changing water levels and to accurately delineate the floodwaters on any given day [Schlaffer *et al.*, 2016].

4.3.1. Single Image

A histogram thresholding approach is the simplest and most straightforward single-image classification method. It consists of assigning to the semantic class “flooded” all pixels with a backscattering value lower than a given threshold. To overcome the subjectivity of this method, many automated techniques have been proposed in the literature. They are based on either parametric or non-parametric approaches.

When the former are applied, water and all other classes are discriminated by approximating the class distributions with predefined statistical models and, as a result, the optimal threshold value can be derived from their parameters. By contrast, the nonparametric approaches do not make any assumption about the classes' statistical distributions. In 2007, Bazi *et al.* [2007] introduced a representative variant of a parametric thresholding approach that consists of automatically estimating the statistical parameters of the “target” and “background” classes by the expectation-maximization algorithm. The approach is based on the assumption that the two classes both follow a generalized Gaussian distribution.

One of the most widely used nonparametric image thresholding techniques is known as Otsu's method. It searches for the threshold that minimizes within-class variability while at the same time maximizing between-class variability [Otsu, 1979]. The main advantage of this approach is that it is computationally inexpensive and therefore particularly suitable for rapid mapping applications. For calm open water surfaces, the results of thresholding approaches are usually reliable and the largest part of an inundation area is detected.

However, the effectiveness of pure thresholding methods is reduced when the “target” and “background” classes are unbalanced and/or overlap significantly. This is often the case as flooded areas typically cover a relatively small fraction of a SAR scene and different

factors contribute to having relatively high backscatter from inundated terrain. A procedure adopted to render thresholding approaches more robust consists of splitting the entire SAR scene into different tiles that were either manually or automatically selected for their bimodality characteristics [Chini *et al.*, 2017; Martinis *et al.*, 2009; Martinis *et al.*, 2015c].

To limit the over- and under-detection of flooded areas, backscattering thresholding is sometimes complemented with contextual information. A possible approach to do it is region growing, which is an image segmentation method that starts with the selection of seeds, which are usually identified via thresholding. The procedure then examines the backscatter values of neighboring pixels in order to determine whether they should be added to the “flood” class or not. A recent example of such an approach is provided in Giustarini *et al.* [2013].

Active contour modeling is an alternative that allows converting incomplete or noisy edge maps into smooth continuous vector boundaries [Mason and Davenport, 1996]. An automated technique for delineating a fluvial flood using a statistical active contour model was first described in Horritt [1999]. The proposed approach is applied to a SAR image to identify areas of homogeneous speckle statistics. The approach was further developed by Mason *et al.* [2007] where SAR image information was supplemented with topography data and vegetation height maps. As a result, the ground height of the edge points of the flood map varies smoothly along the river reach. A hybrid region growing and active contour modeling approach was adopted by Mason *et al.* [2010].

4.3.2. Multitemporal Image Analysis

A second category of flood mapping algorithms is based on the analysis of two or more SAR scenes acquired over time. In its simplest form, a change image is produced by subtracting the grey values of a flood scene from those in a so-called reference image acquired before the event. Changes in backscatter are assumed to be mostly due to the appearance of floodwater and the delineation of the latter requires the application of a classification algorithm to differentiate the “target” (i.e., changed pixels) and “background” (i.e., unchanged pixels) classes derived from the difference image [Chini *et al.*, 2013, 2008].

A variety of algorithms are available to distinguish the changed and unchanged areas from a pair of SAR scenes. The previously described thresholding algorithms represent an option. A more advanced split-based approach for unsupervised change detection was proposed by Bovolo and Bruzzone [2007], for the identification of tsunami-induced changes obtained from multitemporal SAR imagery. A fully automated hierarchical split-based approach was introduced by Chini *et al.* [2017], which

searches for tiles that are characterized by histograms of backscatter and change values depicting both an observable bimodality. The process facilitates the parameterization of the two distribution functions, thereby rendering the mapping of the floodwater more accurate and reliable.

The application of change detection requires the availability of SAR scenes acquired under nonflooded conditions. To select an adequate reference image, several requirements should be fulfilled: the reference image should have the same viewing geometry and the same polarization configuration as the selected flood image. Furthermore, it should have been acquired during the same season as the flood image, especially for applications in regions characterized by a pronounced seasonality in moisture and vegetation growth. The difficulties of finding an adequate image in the archive and of correctly interpreting all detected changes in backscatter represent the main limitations of flooding-related change detection. The advent of missions such as Sentinel-1 providing regular observations at high temporal resolution together with the development of algorithms rendering the retrieval of reference images automatic and objective [Hostache *et al.*, 2012] facilitates the application of these techniques.

Methodologies based on interferometric SAR are starting to be more widely used for flood mapping. These methods also fall in the category of change detection techniques. A well-known problem of SAR-based flood mapping is that the detection of floodwater in built up areas remains problematic. This is because the increase of the double-bounce effect resulting from the presence of floodwater between buildings is hardly detectable through the observation of changes in SAR intensity. To address this important issue Refice *et al.* [2014] and Pulvirenti *et al.* [2015] developed algorithms that integrate SAR intensity data with other features extracted from SAR data, such as the coherence. The interferometric coherence is basically a measurement of the degree of correlation between two complex (phase and amplitude) SAR images. It is particularly related to the change in the spatial arrangement of the scatterers within a SAR image pixel [Chini *et al.*, 2015], and thus to geometric changes in the scene. Flooded areas exhibit low coherence, which helps distinguishing them from nonflooded regions where coherence tends to be high. A coherence-based change detection approach thus effectively complements one that is solely based on intensity change detection.

The launch of several constellations of SAR satellites paves the way to improve flood mapping by making use of multitemporal as well as multi-angular information. An approach that is based on a time series of backscatter derived from tens or hundreds of images acquired over an area allows characterizing floodplains in an unprecedented

way. Notwithstanding this recent progress, multitemporal image analysis of SAR data is still the exception rather than the rule and these techniques are mostly applied to optical data.

In their pioneering study Westerhoff *et al.* [2013], used multitemporal ASAR imagery to estimate for each pixel specific probability distributions of water and nonwater backscatter. Using these histograms, the probability of a “new” measurement belonging to either one or the other population is derived. In O’Grady *et al.* [2014], collections of SAR data were used to find a relationship between local incidence angle and backscatter coefficient, which is used to separate water and nonwater pixels, thereby addressing commonly encountered problems with single image techniques and simpler forms of change detection such as underdetection due to waves on water and over-detection due to low backscatter from dry surfaces. A harmonic model was fit to the backscatter time series on a per-pixel basis and used to generate flood maps from newly acquired SAR scenes in Schlaffer *et al.* [2015].

4.4. IMAGE INTERPRETATION: CHALLENGES AND SOLUTIONS

The contrast between water and land backscatter values is caused by specular reflection, which decreases the backscatter returned to the sensor. This allows for the use of thresholding procedures, as the overlap between class histograms is not significant [Martinis *et al.*, 2009; Martinis *et al.*, 2015a; Boni *et al.*, 2016]. These techniques work fairly well for surface water extraction in relatively homogeneous regions such as bare soils. However, as discussed in the previous section, natural environments are rarely so ideal. Flood surfaces are mostly broken by emergent vegetation, roughened by wind effects or by protruding urban structures, each of which contribute to complex scattering responses (Fig. 4.4).

As backscatter is affected by all the factors discussed above, inferences based solely on the signal return are often ambiguous. Motivated scientific research in this direction has resulted in some remarkable improvements, however, many open research questions remain. In this section, the challenges in SAR-based flood delineation and state of the art solutions proposed in literature are discussed.

4.4.1. Open Water Surfaces

4.4.1.1. Smooth Water Detection

From the theoretical concepts presented in section 4.2.2, it is clear that the case where the water surface is substantially smoother than the adjacent land pixels at the boundary is ideal for surface water detection. For such areas, in which this difference in backscatter values

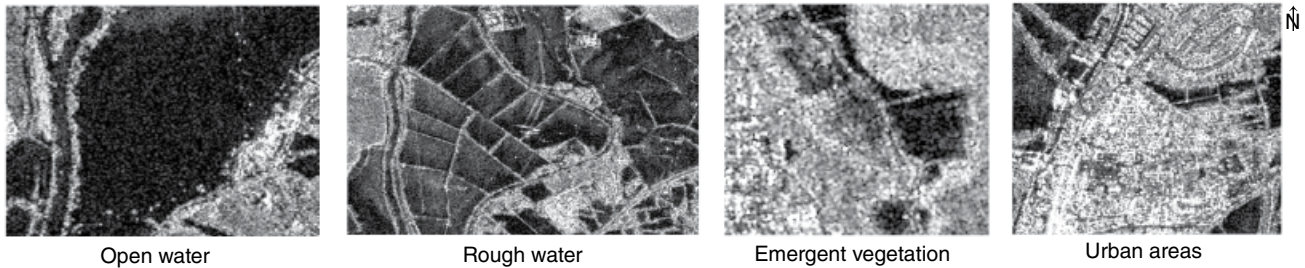


Figure 4.4 The image shows example subsets of problem areas in SAR-based flood mapping taken from a TerraSAR-X (HH, 3-m Stripmap) scene acquired on 25 July 2007 covering the Severn River flood event. The urban area shown here lies to the west of Tewkesbury, UK. © 2007 DLR, adapted from *Mason et al.* [2012].

allows a clear distinction between land and water, many approaches have been proposed in literature. Some of the most common ones include visual interpretation, histogram thresholding [Matgen *et al.*, 2004], automatic classification algorithms like active contour (snake) [Horritt *et al.*, 2001], and contextual classification [Martinis *et al.*, 2011], which have been reviewed most recently by Grimaldi *et al.* [2016] and Brown and Brownett [2016]. Some hybrid automated techniques featuring backscatter modeling, radiometric thresholding, region growing, and change detection have been proposed to simplify the processing of large number of data sets in a near-real-time manner [Matgen *et al.*, 2011; Giustarini *et al.*, 2015a].

Most of the methods listed above work very well for smooth water detection in near ideal cases. Roughness and smoothness are a function of wavelength and angle of the incident radar beam. With present understanding, it intuitively follows that lower wavelength or higher frequency systems display a higher land-water backscatter contrast ratio leading to better detection of smooth open water. The sensitivity to surface roughness is drastically reduced with increasing wavelengths, as many of the potential scatterers on land also appear smooth to the low frequency sensor, which in turn leads to a reduced contrast between flood and nonflood classes.

The contrast between these two land-cover classes increases with the incidence angle, as the scattering from a smooth surface decays more rapidly than that of a rough surface, as a function of the incidence angle [Wdowinski *et al.*, 2008; Weydahl, 1996]. The drawback of working with higher incidence angles is an increase in the shadow effect or regions where an object point is not reached by any portion of the radar beam [Kropatsch and Strobl, 1990]. This effect is caused primarily by the side-looking imaging technique of SAR system and primarily occurs in areas with steep reliefs or in the presence of obstacles such as buildings. As the radar views objects at an angle, it cannot see a certain region hidden by vertical structures, these appear as dark shadows in the SAR image. This can give rise to some false alarms since its backscattering values are similar to that of water.

Moreover, if the incidence angle is reduced, the layover effects that occur may mask the view of hydraulically important features leading to loss of important domain knowledge and underestimation. As the spatial resolution is continuously improved with newer SAR sensors joining the fleet of EO satellites every year, the size of objects that can cause such distortions is getting smaller. For example, in high-resolution imagery, riparian vegetation can cast a shadow over the flooded area boundary being detected and add uncertainty to various regions.

Change detection approaches that use the difference between a pre-flood and post-flood image acquired with the same geometric characteristics are often used to deal with this problem as shadowed areas show the same backscattering values. In some cases, the same considerations can apply for very smooth urban surfaces such as tarmac or asphalted areas. However, the shadowed area remains a region where no information is available and, thus, hydraulic models or other ancillary data must be used to fill the gap [Pierdicca *et al.*, 2008].

The shadow effect can also be precalculated if a high resolution DEM is available to calculate the local incidence angle at each pixel (i.e., incidence angle with respect to the local normal to the surface). Then, a map of areas in shadow, which occurs when the local incidence angle is larger than $\pi/2$ rad, can be precomputed to avoid false alarms. One of the more recent approaches suggest using linear regression to derive the slope coefficient between the local incidence angle and backscatter. The study found that the class separability was much higher when using the derived coefficient in place of backscatter [O'Grady *et al.*, 2013]. The only limitation of this study was the data-intensive approach, which requires enough samples of contemporary SAR images to assess the variation in backscatter behavior with the local incidence angle, which may not be available for most study areas.

In terms of polarization, several studies have assessed the best combination of transmitted and received polarizations for smooth open water detection. As one might expect, the horizontal component of the beam undergoes a perfect specular reflection resulting in low signal

returns. Conversely, vertical polarizations are extremely sensitive to surface roughness, especially at higher frequency ranges [Barber *et al.*, 1996]. This means that a short wavelength radar beam would experience severe scattering over “rough” land surfaces. Although all polarizations can be used for flood mapping of bare terrains, VV is more sensitive to the small waves generated by the wind over a water surface, while the wind effect for flood detection is somewhat mitigated in HH polarization. Wind-induced surface roughening is one of the major causes of underdetection due to the reduced contrast between backscatter from flooded and nonflooded soils.

The contrast between flood and nonflood regions is usually larger for moist soils, because the volumetric soil moisture content increases the complex soil permittivity. This results in an increase of the contrast between the electromagnetic impedances of air and terrain. In fact, for a constant roughness, backscatter increases with an increase in soil moisture [Pierdicca *et al.*, 2008; Panegrossi *et al.*, 2011]. Moreover, because soil permittivity and roughness play the same role for both water and land, the difference in backscattering between floodwater and bare soils is not largely affected by frequency. Although in case of a very calm water surface, the contrast may increase with frequency, as the soil would appear equivalently rougher to the sensor and therefore appear brighter in the image. At this point, it would be worthwhile to recall the concept of roughness, which needs to be considered relative to the radar wavelength. A surface considered smooth at lower frequency (e.g., L-band) may behave as a rough surface at higher one (e.g., X-band).

4.4.1.2. Rough Water Detection

Flooded SAR images are often captured while the associated rainfall event is ongoing, which implies that open water surfaces are roughened due to wind and rain effects. Larger water surfaces like oceans are more susceptible to the effects of wind, which generates small amplitude waves over a wide range of wavelengths resulting in Bragg scattering. Smaller inland water bodies such as lakes, reservoirs, or flood inundation patches, exhibit a more irregular pattern of roughness leading to some diffuse surface scattering. These factors, which increase the surface roughness, result in higher signal returns, which in turn reduce land-water class separability and could potentially lead to an underestimation of the flooded area.

Wind-induced gravity waves are still an open issue in case of mapping inland water from SAR because many unknown factors (different depths or obstacles that screen the wind flow) contribute to the problem. This makes modeling the radar signal rather challenging, even in case accurate meteorological information is available. The linear regression approach proposed by *O’Grady*

et al. [2013] to enhance separability between water and lookalike surfaces, which exhibit specular scattering behaviors, was extended to solve this problem. Additional parameters like backscatter normalized to 30° (using the fitted model) and the ratio between standard deviations of the time series of backscatter and intercept (SDR) at each pixel, was additionally used to derive a thresholding-based flood map [O’Grady *et al.*, 2014]. Optimally, thresholding the SDR image showed the best class separability, establishing the merit of generating such a database globally. Currently, operational and planned high-resolution SAR missions facilitate the development of such a database in the future.

In addition to wind roughening, intense precipitation events [Pulvirenti *et al.*, 2012] and wet snow [Pulvirenti *et al.*, 2014a] also contribute to flood detection problems. The signal attenuation caused by heavy rain can be observed at higher frequencies, since the amount of absorption and scattering of the signal due to water drops is higher. Similar to the case of rain, wet snow is also very absorbent and produces very low backscatter, which can be easily misinterpreted as floodwater [Pulvirenti *et al.*, 2014a]. Ancillary data such as local incidence angle maps, land cover maps, and optical imagery, can be utilized to supplement SAR information and reduce false alarm errors arising from this phenomenon [Pulvirenti *et al.*, 2014a].

4.4.2. Partially Submerged Vegetation

Identifying flooding in pixels having a high vegetative fraction is relatively harder due to the complex scattering patterns that result. Double-bounce scattering represents the key process that is used to detect flooded vegetation on a SAR image. Radar beams achieve measurable penetration depths directly proportional to the incident wavelength. When the ground is covered by a smooth and very reflective water surface, the intensity of the double-bounce effect increases notably depending on canopy penetration. The returned signal is a combination of dihedral reflection caused by steep emergent stems for the parts of the radar beam that surpass the canopy, and volume scattering, resulting from the radar beam traveling through air, interleaved with a multilayer canopy, all having different electrical permittivities [Richards *et al.*, 1987]. However, the difference between the signal returned by a flooded and a nonflooded forest is strongly dependent on vegetation and sensor characteristics.

The abovementioned factors result in volume scattering, which negates specular reflection effects and reduces detectability of flood patches. SAR sensors operating in the longer wavelength regions can partially penetrate vegetation canopies, as penetration is directly related to the signal wavelength. Additionally, the double bounce

can be exploited to detect the flooding, as nonflooded forested areas would return a lower backscatter due to the underlying rough forest floor, which does not support corner reflection mechanisms [Pulvirenti *et al.*, 2013]. In this case, an increase in soil moisture content decreases the contrast with flooded vegetation because the double-bounce effect gets amplified.

Flooded vegetation often results in enhanced backscatter due to a combination of dihedral and volume scattering, as opposed to dry vegetation where the radar beam only undergoes volume scattering. A review of early studies investigating flooding under vegetation concluded that L-band radar images exhibited higher sensitivity to detect flooding under vegetation [Hess *et al.*, 1990], and that steep incidence angles are better for flood detection as the possibility for the radar pulse to reach the forest floor is increased. Increasing the incidence angle also raises the bistatic surface scattering, however, smaller angles favor larger penetration depths. It is critical then to determine the optimum angle of incidence for the specific domain application being considered, such that the double-bounce enhancement effect is most pronounced.

As longer wavelengths favor greater penetration depths, they are often preferred for monitoring floods in vegetated areas. However, several studies have demonstrated that C-band data could allow flood mapping under lighter canopies [De Grandi *et al.*, 2000]. Another factor affecting the penetration depth for forested regions outside the tropics is seasonality. As the shedding of leaves reduces the potential scatterers in each pixel, lower wavelength sensors can also achieve penetration during leaf-off seasons [Townsend, 2001]. This has been examined by using X-band data to investigate surface water extent under low-density canopies [Antonova *et al.*, 2016]. An increase in backscatter was noted for all the different forest types in that area under flooded conditions indicating that such approaches could be useful for boreal and temperate environments [Voormansik *et al.*, 2014; Cohen *et al.*, 2016]. For cases of increasing complexity where flooded water needs to be distinguished from marshes or mangroves, using multifrequency fully polarimetric data and the use of P-band is suggested for high-density canopies [Martinis and Rieke, 2015].

Although radar polarimetry can facilitate a reliable detection of the complex scattering mechanisms observable in flooded vegetation, fully polarimetric SAR images are often unavailable during a flood event. Polarimetry is able to isolate the contribution of the double bounce from volume and surface scattering mechanisms, which is beneficial for detecting the changes caused specifically by flood water. This is done by measuring the magnitude and phase difference between copolarized (i.e., HH, VV) and cross-polarized (e.g., HV backscatter) backscatter [Plank *et al.*, 2017].

It was also demonstrated that using a combination of HH and VV polarized images favored the separation of flooded and unflooded forests over the use of HH data alone [Zalite *et al.*, 2014]. This can largely be attributed to the increased phase difference observable in the former, as a result of interactions with inundated vegetation. In case of dense vegetation, the combined occurrence of absorption and scattering can produce an overall attenuation that is relevant also for the HH polarization. In such cases, the SAR signal is reduced as the biomass increases, penalizing especially higher incidence angles and creating false alarms as well, since the backscattering is drastically reduced.

More recent studies proposed the use of interferometric SAR (InSAR), which measures the level of similarity between two SAR images based on the speckle distribution patterns. Recall that speckle results from multiple scatterers within the same ground resolution cell, meaning that this pattern should be consistent for a given geographic area imaged using identical sensor characteristics. If the difference in acquisition times of the SAR images can be limited such that the only change in terrain properties to occur within that duration is the flooding, coherence data can supplement intensity information for flood detection under canopies [Refice *et al.*, 2014].

Vegetation normally decorrelates the microwave signal intensities due to volume scattering, which determines low Differential SAR Interferometry (DInSAR) coherence (even for short temporal baselines). This is primarily a result of changes in plant phenology and movement of stalks and/or leaves caused by wind. However, flooded vegetation is characterized by even lower values of coherence due to the added presence of floodwaters [Chini *et al.*, 2012]. Flooded waters contribute further to decorrelation due to specular reflection properties, which in the presence of emergent vegetation manifests as double-bounce scattering [Zebker and Villasenor, 1992]. When combined with intensity information, flooded vegetation can be identified as areas displaying an increase in backscatter and decrease in coherence [Nico *et al.*, 2000]. These approaches primarily detect the change in image texture and dielectric properties, which can be explained as a function of the underlying water level [Pulvirenti *et al.*, 2011a]. As the use of these change detection approaches are very sensitive to the temporal baseline of the SAR acquisitions, the use of newer satellites offering relatively lower repeat cycle, like the COSMO-SkyMed (CSK) Constellation, should be explored.

The problem with high-frequency SAR systems like CSK is the heightened sensitivity to any potential scatterers. However, for narrow-leaved plants, these data could still provide useful information [Pierdicca *et al.*, 2017]. Furthermore, the capability to provide multitemporal

observations can support the monitoring of flood evolution in some areas. If the land-cover distribution of the vegetated areas in the scene is known a priori, vegetation scattering models can be used to predict backscatter behavior [Pulvirenti *et al.*, 2011b]. This information assists in tuning fuzzy models, which can then be used to interpret flooded vegetation while simultaneously acknowledging the uncertainty [Pulvirenti *et al.*, 2013].

4.4.3. Urban Flooding

Flood detection around urban features is challenging due to a variety of factors. Double-bounce scattering from buildings and pavements, along with metals with high dielectric constants having high reflectivity, contribute to the enhanced backscatter observed. The effect of material properties dominates over the soil roughness characteristics, since the smooth urban surfaces like tarmac and asphalt are already smooth with respect to still water [Mason *et al.*, 2010]. Distortion effects caused by the side-looking sensor geometry additionally pose problems for high to very high resolution SAR imagery as high-rise buildings tend to cause shadows and layover effects [Mason *et al.*, 2012b].

Smooth urban surfaces cause specular reflection and return a signal, very similar to inundated areas, frequently leading to false alarm situations. However, it must be noted that specular reflection effects are increased for smooth urban surfaces oriented along the sensor's line of sight. Conversely, corner reflection is more likely to occur if the urban features are oriented orthogonally to the incoming radar beam [Pulvirenti *et al.*, 2015].

Change detection (CD) based approaches were found to reduce the misclassifications of other dark image regions by identifying areas of shadow, layover, tarmac, and permanent water a priori [Giustarini *et al.*, 2013]. Once these areas are diagnosed and masked out, overestimation can be substantially lowered. Earlier studies investigated the use of active contours in conjunction with region growing. However, each step of the seed selection process required manual intervention. Further studies automated this seed selection process for region growing using LiDAR-based topographic information [Schumann *et al.*, 2011].

While backscatter based approaches like change detection can work in some case studies [Aggarwal *et al.*, 2014], there are some limitations for urban flood detection problems. For instance, the backscatter variation attributable to a change in the surface dielectric constant, which is caused by the flooding, is nearly unobservable as the returned signal is too low due to specular reflection. If the smooth tarmac surfaces like roads and pavements are masked out of the analysis, flooding on and around these features cannot be detected [Pulvirenti *et al.*, 2015].

Conversely, in the case of dihedral reflection, this intensity change is usually detectable, as the increased surface reflectivity results in a stronger return. However, if the water level is not negligible with respect to the building height, the signal return from corner reflectors might be reduced due to a decrease in the beam cross-sectional area [Thiele *et al.*, 2007]. Therefore, the reliability of SAR intensity-based approaches appears to be limited for operational urban flood mapping.

The interferometric coherence approach discussed in section 4.3.2 has recently been applied to deal with many of these limitations. Urban areas are generally temporally coherent as the decorrelation is a function of relative motion of scatterers in the pixel over the temporal baseline (separation between the two image acquisitions), which can be considered negligible for high-density built-up areas. On average, double bounce in urban regions corresponds to highly coherent targets in the image as a function of their high backscatter in combination with temporal invariance. As spatial decorrelation is inversely proportional to the wavelength of the radar beam, at lower wavelength bands, this effect is more pronounced [Zebker and Villasenor, 1992].

Standing water is expected to decorrelate the signal more than is expected, a property that may be exploited for urban flood mapping [Pulvirenti *et al.*, 2015; Matgen *et al.*, 2011]. In high-resolution SAR imagery, some false alarms in the coherence information may be generated from dynamic traffic flows and parking lots. However, assessing three pairs of SAR images acquired within the critical spatiotemporal baselines, one for the dry or pre-event situation, one with images acquired before and after the event, and finally a postevent pair, can help in correctly identifying the decorrelation caused by flooding. While this seems to be a data-intensive approach at the outset, when the improved temporal resolutions of current and upcoming SAR sensors is considered, it appears more likely that such data may soon be available for analysis globally.

Gaps still remain in urban areas, such as shadowed areas structures where SAR backscattering does not provide any information about the presence of water, and they could be filled up by the assimilation of the flood maps into hydraulic models. In that case, the flood maps should be provided in terms of probability that a certain pixel is flooded in order to characterize the uncertainties associated with the flood map [Panegrossi *et al.*, 2011].

4.5. REPRESENTATION OF UNCERTAINTIES

Regardless of the number of images considered, most SAR image processing methods output flood extent estimates in the form of binary maps and thus do not provide any indication on the uncertainty associated with the

pixel classification. A more informative and arguably more advanced method is to estimate the probability of each pixel belonging to the flood class. However, probabilistic flood mapping is still not very common and only a few noteworthy exceptions exist [Westerhoff *et al.*, 2013; Giustarini *et al.*, 2016; Schlaffer *et al.*, 2017]. Previous studies on the characterization of uncertainties in flood extent maps have often been limited to random realizations of potential sources of uncertainty [Hostache *et al.*, 2006, 2009; Schumann *et al.*, 2008b; Di Baldassarre *et al.*, 2009; Refice *et al.*, 2014; Giustarini *et al.*, 2015a].

The uncertainties contributed by ambiguities in backscattering properties cannot be completely removed [Stephens *et al.*, 2012]. Approaches that account for this uncertainty in the flood detection process provide fuzzy outputs in which pixel values convey the confidence with which the pixel is correctly classified as flooded. As SAR-based flood extents serve as calibration and evaluation targets for hydrodynamic models, quantifying the uncertainty of flood observations is essential [Schumann *et al.*, 2008]. Studies have successfully illustrated that factors like the acquisition time of the SAR image [Gobeyn *et al.*, 2017], sensor characteristics [Giustarini *et al.*, 2015a], as well as the flood mapping procedure chosen [Di Baldassarre *et al.*, 2009] can impact the calibrated model parameters. These studies demonstrated the need for a shift toward probabilistic mapping, which is the current consensus in the flood mapping community [Di Baldassarre *et al.*, 2011, 2010; Schumann and Di Baldassarre, 2010; Alfonso *et al.*, 2016].

The discussion in the previous section of factors that may contribute to errors in SAR-based flood maps is important to understand and identify areas in which the model outputs will always be more reliable. However, in practical applications, when large amounts of data need to be processed, especially at the regional or global scale, it makes more sense to convey the observational uncertainty to the model for which several techniques have been proposed in literature.

For example, Schumann *et al.* [2008] investigated uncertainty in SAR-derived water stages, for a single SAR image and a single flood mapping procedure, and identified two main sources of uncertainty: (1) the parameter value applied to classify a pixel as flooded (i.e., flooded/nonflooded classification threshold) and (2) geocoding of the image itself. The study conducted by Refice *et al.* [2014] implicitly introduced a semiautomated approach that allows integrating ancillary information to derive a posteriori probabilistic maps of flood inundation, accounting for different scattering responses to the presence of water.

In order to eliminate the subjectivity in the selection of a particular algorithm for flood mapping, several studies investigated the use of a possibility of inundation (POI)

map [Schumann *et al.*, 2009; Schumann and Di Baldassarre, 2010; Di Baldassarre *et al.*, 2009]. An ensemble of maps generated using a variety of flood detection algorithms that perform equally well for a given study region are combined to arrive at the POI map. Each pixel in the POI map is assigned a value between 0 and 1 based on how many of the ensemble members classified it as flooded. It can be interpreted as an event-specific flood probability map, which can facilitate probabilistic calibration procedures.

Fuzzy approaches that combined SAR-based information with available ancillary data sets have since been suggested and exploited for operational flood mapping at various levels [Pulvirenti *et al.*, 2011b; Pierdicca *et al.*, 2008; Pulvirenti *et al.*, 2013; Pappenberger *et al.*, 2007]. The fuzzy membership functions are usually defined based on EM backscattering models for each land-use class the classifier may encounter in the SAR scene. These models can be difficult to parameterize if domain knowledge is limited, thus histogram based methods still need to be tested for more generalizability.

Probabilistic mapping approaches that utilize Bayesian posterior probabilities of flooding to each pixel were tested recently, demonstrating a good agreement with the validation data assessed through reliability diagrams [Schlaffer *et al.*, 2017; Giustarini *et al.*, 2016]. One of the major limitations of current validation strategies is that the validation data are assumed to be completely true. This is counterintuitive as probabilistic mapping operates on the premise that observational uncertainty needs to be acknowledged. The current challenge is to develop an effective statistical measure to assess fuzzy flood maps with fuzzy validation data.

4.6. CASE STUDIES

The following section describes a few of the various innovative SAR-based flood mapping techniques proposed in state of the art literature [Addabbo *et al.*, 2016; Arnesen *et al.*, 2013; Avendano *et al.*, 2015; Boni *et al.*, 2016, 2015; Policelli *et al.*, 2017; Ahamed *et al.*, 2017; Chaouch *et al.*, 2012; Cossu *et al.*, 2009; Twele *et al.*, 2016]. Operational flood mapping approaches that utilize data from more recently launched high-resolution sensors, as well as older coarser resolution satellites, have been selected here as the two case studies to reflect the current progress and continuing challenges at various spatial scales. The first study proposes a framework for planning satellite data acquisitions at opportune moments across the hydrograph, based on flood forecasts [Boni *et al.*, 2016]. The sensors tested for preliminary analysis were COSMO-SkyMed and Sentinel-1, both of which provide high-resolution SAR imagery ideal for assessing floods in small to medium-sized catchments. The second study investigates the possibility of delivering a global

high-resolution flood mapping service based on any kind of SAR data, from higher to lower spatial resolution data [Martinis *et al.*, 2015c].

4.6.1. A Prototype System Using COSMO-SkyMed and Sentinel-1 Data

4.6.1.1. Background

The study by Boni *et al.* [2016] tried to maximize the flood insights gained from multiple sensors with high spatial and temporal resolutions, by testing a combination of data sets from the CSK and Sentinel-1 constellations. Flood Early Warning Systems (FEWS) can be used to plan SAR acquisition at optimal temporal instances across the hydrograph in advance. Another important contribution that FEWS can make is to help identify the regions in which large area-wide swath imagery can sufficiently characterize the flooding for on-demand very high-resolution acquisitions over areas of complexity. Additionally, the Near Real Time (NRT) SAR-based flood mapping algorithm proposed in Pulvirenti *et al.* [2014] for COSMO-SkyMed imagery was adapted for Sentinel-1 data to ensure transferability and robustness.

4.6.1.2. Methodology

The areas of interest (AOI) for satellite SAR acquisitions were selected based on the forecasts of water levels and discharge generated by the FEWS. Currently, this AOI prioritization is done by a joint team of experts with representatives from all stakeholder organizations based on flood forecasting, risk management, and remote sensing perspectives. As illustrated in Figure 4.5, the wide swath, high-resolution, Sentinel data can characterize the floodplain involvement quite clearly, while the very-high-resolution CSK data allow a temporal assessment of critical areas.

The NRT mapping algorithm used a split-based approach, which divided the SAR image into nonoverlapping subsets, with land-water thresholds automatically selected from the ones that exhibit bimodality in the image histogram. The average of all the subimage thresholds was used as the global threshold and finally a region growing algorithm was used to generate the flood map.

4.6.1.3. Observations

The NRT flood maps generated were quantitatively compared to the flood hazard map generated by the hydraulic model embedded in the FEWS set up for River Po, through the user's accuracy, which was found to be consistently above 60%. However, the user's accuracy only provides an estimate of the commission errors, which simply assess where the mapping approach overestimates. Areas of underestimation are essentially neglected by this performance measure. Therefore, a full

accuracy assessment was conducted against a small cloud-free subset of Landsat-8 optical data, the results of which are summarized in Figure 4.6. The user's accuracy and producer's accuracy for this analysis were 69% and 72%, respectively, which indicates that the algorithm is sufficiently reliable for emergency response.

One of the major challenges in the selected study area was the presence of flooded vegetation. An investigation of the different available polarizations revealed that the Sentinel-1, cross-polarized data were better able to capture the flooding under vegetation. It is important to note that these approaches can be applied only when preflood images are available to facilitate change detection, or a multitemporal, multisensor, fully polarimetric data set is available for flood assessment. As the study attempts to guide an acquisition planning that can enable efficient flood monitoring, one can imagine that in the future it may be possible to obtain SAR data according to specific requirements of a particular study area.

4.6.2. A Fully Automated and Efficient SAR-Based Flood Mapping Algorithm Combining Hierarchical Split-Based Approach and Change Detection

4.6.2.1. Background

The study by Chini *et al.* [2017] proposes an unsupervised and fully automatic algorithm for retrieving flooded areas from a SAR image and a SAR change image. It can be seen as a further improvement of the algorithm initially proposed by Matgen *et al.* [2011] and further developed by Giustarini *et al.* [2013]. The latter is composed of a sequence of thresholding, region growing and change detection steps. In order to choose the best available reference image for change detection Giustarini *et al.* [2013] proposes to follow the guidelines provided in the study by Hostache *et al.* [2012]. The change detection step is necessary for differentiating flood water from permanent water and to limit over-detection. The method proposed in Giustarini *et al.* [2013] is unsupervised as the initial calibration of the open water backscatter probability density function (PDF) is only based on the flood image histogram. It is moreover automatic as the threshold values, for the three abovementioned steps are optimized through an automatic iterative optimization process. However, the method proposed by Matgen *et al.* [2011] and Giustarini *et al.* [2013] can fail in calibrating the open water backscatter PDF when floodwater only covers a small part of the image as the histogram is then not clearly bimodal, which is unfortunately quite common when dealing with flood images (floodwater is often only visible on very limited areas of the complete SAR scene). To circumvent this limitation, the study by Chini *et al.* [2017] proposes a hierarchical split-based approach (HSBA-Flood) that allows for calibrating both open

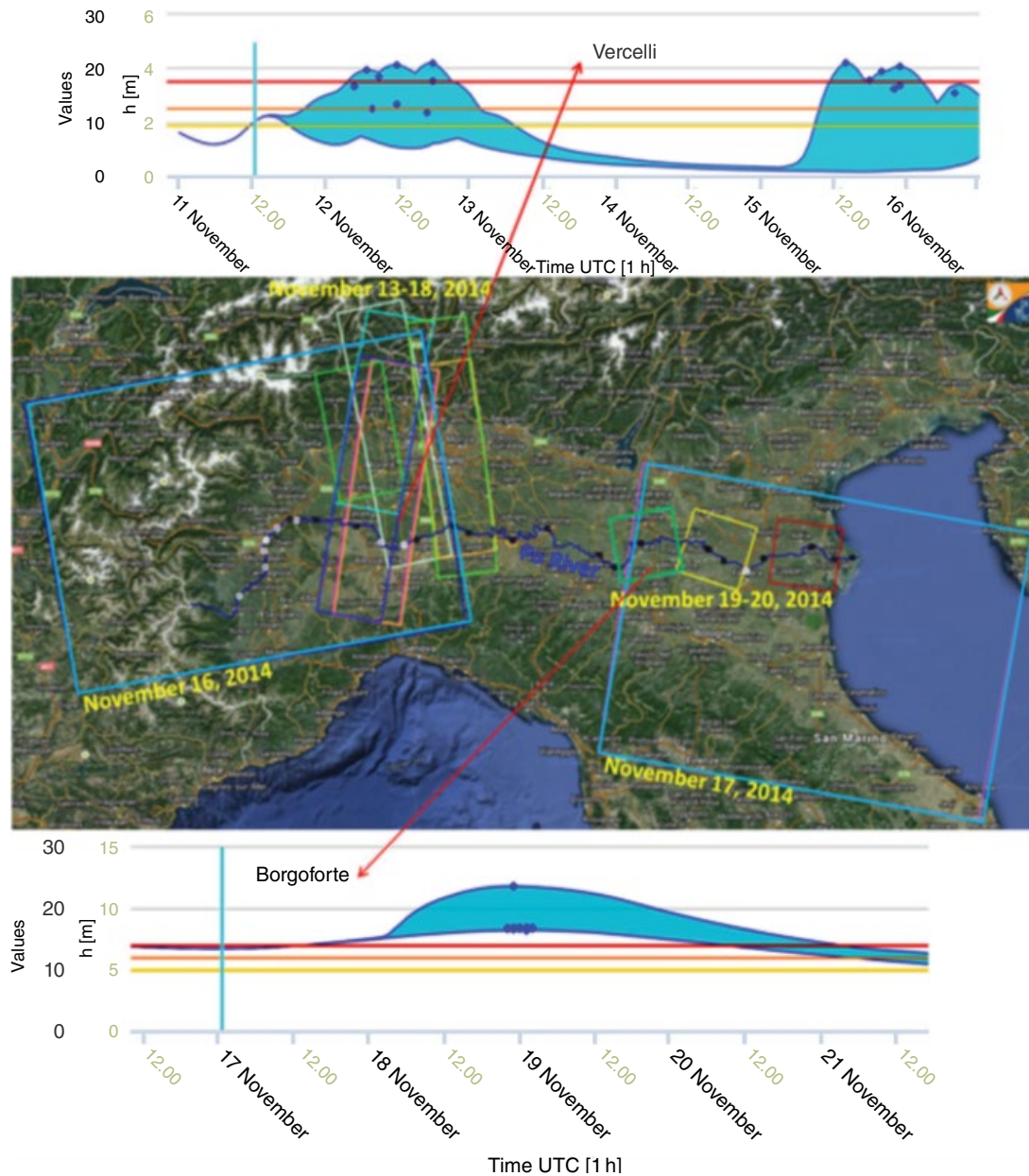


Figure 4.5 Swaths of the CSK (different colors) and S1 (turquoise) images of the area hit by the November 2014 Po River basin event. Two predictions of the FEWS-Po model available through the DEWETRA platform are also shown. The horizontal red line corresponds to the critical reference flood, while yellow and orange lines indicate intermediate levels of warning. Western part of the Po River basin: run of 11 November 2014, h: 12:30 UTC. Eastern part of the Po River basin: run of 17 November 2014, h: 00:30 UTC. From *Boni et al.* [2016]. (See electronic version for color representation.)

water backscatter and flood-induced backscatter change PDF even in the event the area covered by the floodwater is really small compared to the complete SAR scenes.

4.6.2.2. Methodology

To cope with flood extents only covering a small part of the entire SAR scene *Chini et al.* [2017] proposes a hierarchical split-based approach (HSBA) where the

scene is iteratively split in to tiles of variable sizes in order to find those exhibiting a bimodal histogram that can be used to automatically parameterize open water backscatter and flood-induced backscatter change PDFs. It is worth mentioning that this approach does not fix the tile size a priori; instead, a hierarchical tiling of the scene is automatically performed, starting from Level 0 with 4^0 tiles (the complete scene), down to the lower L where the

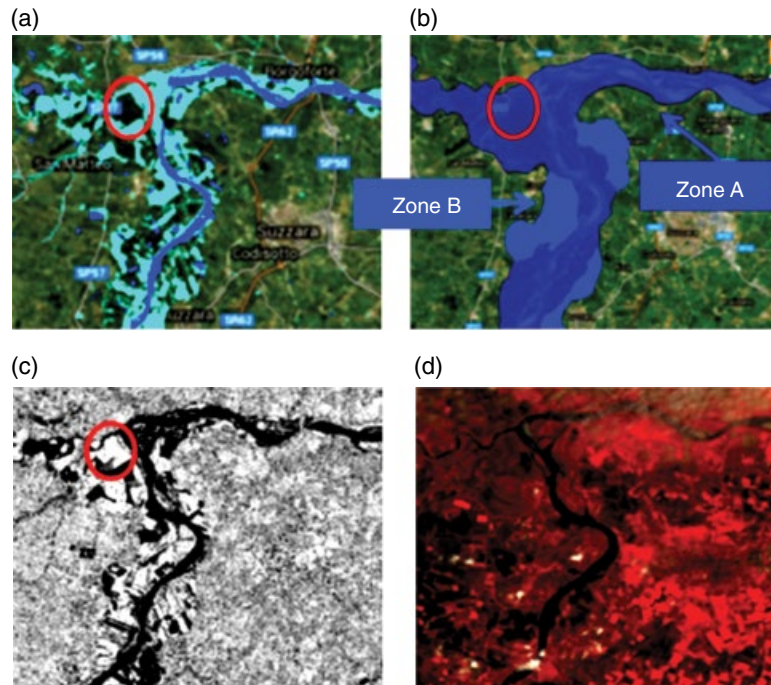


Figure 4.6 Performance assessment of the NRT classification algorithm for (a) CSK-derived flood map and (b) the location of zones A (dark blue) and B (light blue) in the reference map. (c) The CSK intensity image (dB) is displayed. In (d), a false color composite of Landsat 8 for the same area is included. From *Boni et al.* [2016]. (See electronic version for color representation.)

number of tiles is 4^L . The lowest level L is fixed so that the number of pixels included in the level L tiles is sufficient for reliably estimating PDFs. Descending from the upper level (full image) to the lower one (quarters of image, sixteenths of image, etc.), only the tiles that exhibit a bimodal histogram both in the flood and in the change image are selected for parameterizing the PDF of both open water backscatter and backscatter changes due to the flood event, the other tiles being split into four subtiles. For being selected, the tiles have to fulfill the following criteria:

1. The tile histograms (computed based on both the flood and change images) must be bimodal. To evaluate this criterion, the flood image and the change image histograms are first computed for each tile and it is assumed that both are composed of a mixture of two Gaussian distributions. The Gaussian distribution parameters are next assessed using the Levenberg-Marquard algorithm, as implemented in IDL. Eventually, to determine if the Gaussian distributions are well separated, the Ashman D coefficient is computed and values higher than 2 are retained for a clean separation between the two distributions.

2. The smallest population must cover at least 10% of the tile.

3. The population representative of change should have a positive mean value in the change image, meaning

that backscattering in the flooded image pixels is lower than in the reference one.

Based on the statistics of the selected tiles derived from HSBA, the hybrid methodology proposed by *Giustarini et al.* [2013] combining backscatter thresholding, region growing, and change detection is used for the automatic extraction of the flood extent in the entire scene (Fig. 4.7).

4.6.2.3. Results

The approach has been applied on two pairs of reference/flood SAR images acquired by the Envisat and TerraSAR-X satellites during a flood event that occurred in July 2007 over River Severn (United Kingdom). Based on almost synchronous acquisitions of very high resolution aerial photographs (validation data set), the flood extent maps derived in *Chini et al.* [2017] have been evaluated and show very high overall accuracies. Figure 4.8 shows the comparisons between the flood extents derived from Envisat-WS images and TerraSAR-X images against the validation data set.

Moreover, the approach has been recently successfully tested on Sentinel-1 images acquired during flood events. As a result, in collaboration with the European Space Agency's Research and Service Support team, this consolidated flood mapping software is operationally implemented and will be opened as a service in the ESA RSS's Grid Processing On Demand processing (GPOD) environment, where each user

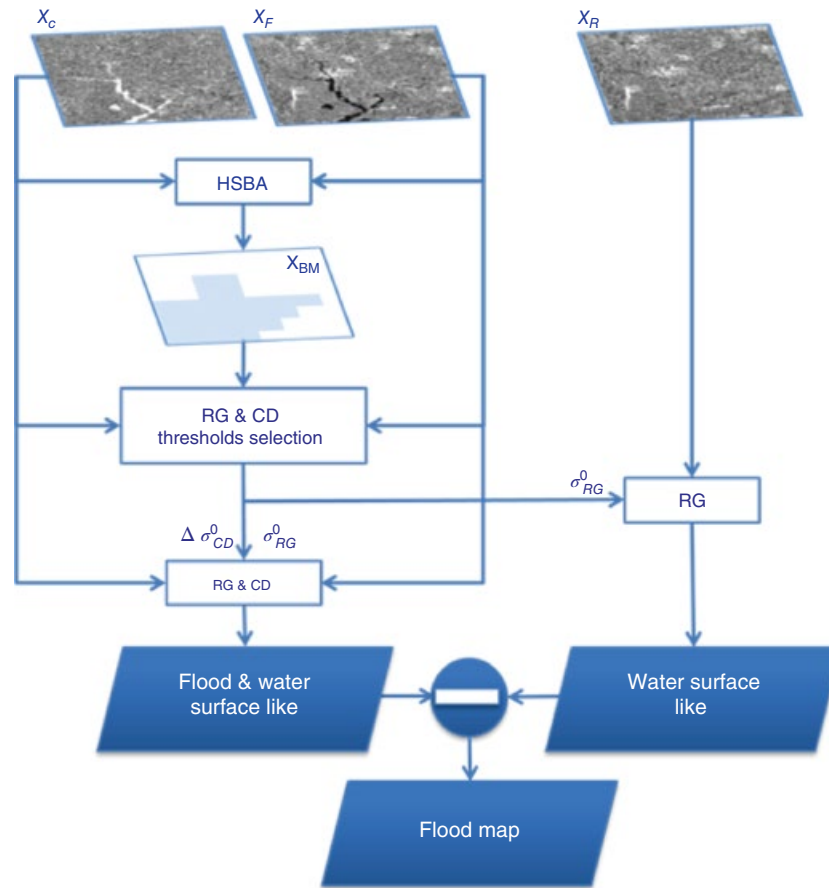


Figure 4.7 HSBA-Flood block diagram. RG: Region growing. CD: Change detection. After *Chini et al.* [2017].

will be able to process the desired data to detect the flooded areas using Sentinel-1 data in an automatic way.

4.7. SUMMARY AND PERSPECTIVES

This chapter provided an overview of the challenges and opportunities associated with operational SAR-based flood mapping at multiple spatial scales. The principles of SAR imaging were discussed with reference to flood detection problems, and the state-of-the-art solutions proposed in literature to eliminate these effects were critically examined. Finally, selected case studies demonstrating the potential of SAR-derived extents for operational flood mapping were presented.

The current generation of high-resolution SAR satellites like COSMO-SkyMed, TerraSAR/TanDEM-X and Sentinel-1, and planned missions like the Radarsat Constellation, NiSAR, TerraSAR/TanDEM-L and CSK-2 have stimulated scientific research on the optimal use of this rich database for flood detection. The shift toward open data policies across space organizations could potentially lead to more innovative solutions to the

persisting challenges in the field and ensure continued investment in satellite SAR technology.

Identifying flooding under vegetated and urban land forms is a research topic of high interest with many open questions currently being examined. The use of ancillary data sets and complementary approaches like interferometric coherence can be helpful. However, diagnostic assessments are required to evaluate the environmental conditions under which each of these approaches work and why. Furthermore, it's important to develop techniques that provide an associated measure of flood detection uncertainties, at least in regions exhibiting complex surface properties.

The shift toward fuzzy and probabilistic approaches in the field of SAR-based flood mapping necessitates the development of suitable validation techniques. Present strategies involve the use of binary validation maps for assessment, which seems counterintuitive, as the premise of this shift from deterministic approaches is that uncertainty cannot be eliminated. Investigative analysis of current mapping approaches for multisensor, multiband data should be conducted across diverse geographical regions to gain an in-depth understanding of why certain approaches favor a particular set of environmental conditions.

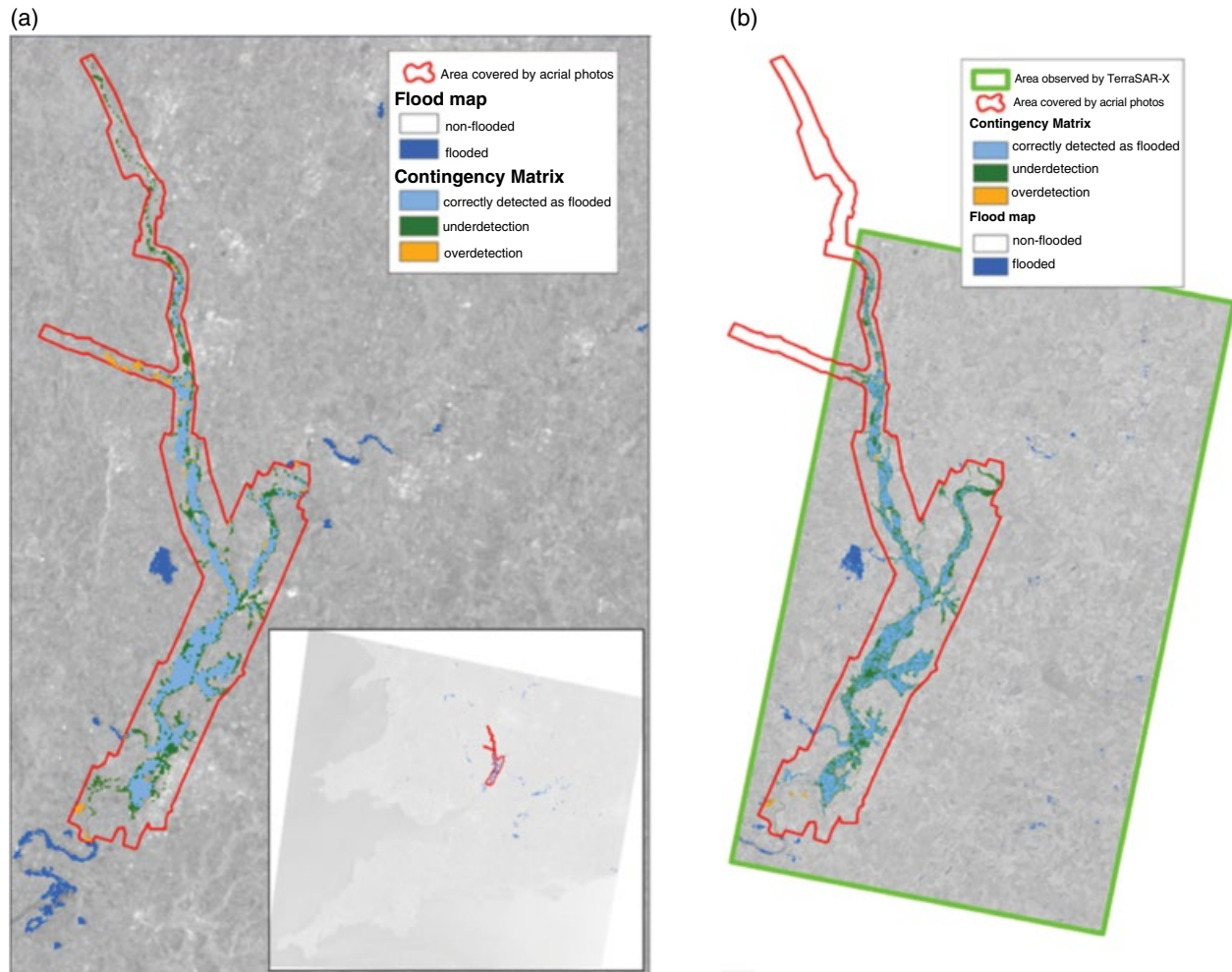


Figure 4.8 Contingency maps between (a) Envisat-WS or (b) TerraSAR-X flood map and validation data set. After Chini *et al.* [2017].

Crowd-sourced flood information has the potential to complement remote sensing based mapping of floods. In addition, the advent of social media and the proliferation of smart phones have ushered in an era of citizen sensing [Fohringer *et al.*, 2015]. However, research in this direction is very new and many scientific challenges remain, especially in the design of validation methodologies. The availability of data from diverse sources will continue to increase in the coming years and the flood mapping community needs to evolve rapidly to unlock the full potential of RS for disaster management.

ACKNOWLEDGMENTS

Antara Dasgupta is funded by the IITB-Monash University Research Academy. The work of Marco Chini, Renaud Hostache, and Patrick Matgen was supported by the National Research Fund of Luxembourg through the MOSQUITO(C15/SR/10380137) project.

REFERENCES

- Addabbo, A. D., A. Refice, G. Pasquariello, F. Lovergine, and D. Via Amendola (2016), SAR / Optical data fusion for flood detection, in *Geoscience and Remote Sensing Symposium (IGARSS)*; doi: 10.1109/IGARSS.2016.7730990.
- Aggarwal, A., F. Rafique, E. Rajesh, and S. Ahmed (2014), Urban flood hazard mapping using change detection on wetness transformed images, *Hydrol. Sci. J.*, 1–10; doi:10.1080/02626667.2014.952638.
- Ahamed, A., J. Bolten, C. Doyle, and J. Fayne (2017), Near real-time flood monitoring and impact assessment systems case study: 2011 flooding in Southeast Asia, in *Remote Sensing of Hydrological Extremes, Near Real-Time Flood Monitoring and Impact Assessment Systems Case Study: 2011 Flooding in Southeast Asia*, edited by R. Escobar C, J. D. Restrepo, G. R. Brakenridge, and A. J. Kettner, 105–118; doi:10.1007/978-3-319-43744-6.
- Alfonso, L., M. M. Mukolwe, and G. Di Baldassarre (2016), Probabilistic flood maps to support decision-making:

- Mapping the value of information, *Water Resour. Res.*, 52 (2), 1026–1043; doi:10.1002/2015WR017378.
- Antonova, S., A. Kääb, B. Heim, M. Langer, and J. Boike (2016), Spatio-temporal variability of x-band radar backscatter and coherence over the Lena River delta, *Siberia. Remote Sens. Environ.*, 182, 169–191; doi:10.1016/j.rse.2016.05.003.
- Arnesen, A. S., T. Silva, L. Hess, E. Novo, C. Rudorff, B. Chapman, and K. McDonald (2013), Monitoring flood extent in the lower Amazon River floodplain using ALOS/PALSAR ScanSAR images, *Remote Sens. Environ.*, 130, 51–61; doi:10.1016/j.rse.2012.10.035.
- Avendano, J., S. F. Mora, J. E. Vera, J. A. Torres, and F. A. Prieto (2015), Flood monitoring and change detection based on unsupervised image segmentation and fusion in multitemporal SAR imagery; doi:10.1109/ICEEE.2015.7357982.
- Barreto, T., J. Almeida, and F. Cappabianco (2016), Estimating accurate water levels for rivers and reservoirs by using SAR products: A multitemporal analysis, *Pat. Recog. Lett.*, 83 (2), 224–233; doi:10.1016/j.patrec.2016.05.015.
- Bazi, Y., L. Bruzzone, and F. Melgani (2007), Image thresholding based on the EM algorithm and the generalized Gaussian distribution, *Pat. Recog.*, 40 (2), 619–634; doi:10.1016/j.patcog.2006.05.006.
- Blasco, F., M. Bellan, and M. Chaudhury (1992), Estimating the extent of floods in Bangladesh using SPOT data, *Remote Sens. Environ.*, 39 (3), 167–178; doi:10.1016/0034-4257(92)90083-V.
- Boni, G., L. Ferraris, L. Pulvirenti, G. Squicciarino, N. Pierdicca, L. Candela, A. Pisani, et al (2016), A prototype system for flood monitoring based on flood forecast combined with COSMO-SkyMed and Sentinel-1 data, *IEEE Journal of Selected Topics in Applied Earth Observations and Remote Sensing*, 9 (6), 2794–2805; doi:10.1109/JSTARS.2016.2514402.
- Boni, G., L. Pulvirenti, F. Silvestro, G. Squicciarino, P. Pagliara, R. Onori, C. Proietti, L. Candela, A. Pisani, and S. Zoffoli (2015), User oriented multidisciplinary approach to flood mapping: The experience of the Italian civil protection system, *International Geoscience and Remote Sensing Symposium (IGARSS), User Oriented Multidisciplinary Approach to Flood Mapping: The Experience of the Italian Civil Protection System*, 834–837; doi:10.1109/IGARSS.2015.7325894.
- Bovolo, F., and L. Bruzzone (2007), A split-based approach to unsupervised change detection in large-size multitemporal images: Application to tsunami-damage assessment, *IEEE Trans. Geosci. Remote Sens.*, 45 (6), 1658–1669; doi:10.1109/TGRS.2007.895835.
- Brown, K., and J. Brownett (2016), Progress in operational flood mapping using satellite synthetic aperture radar (SAR) and airborne light detection and ranging (LiDAR) data, *Prog. Phys. Geog.*, 40 (2), 196–214; doi:10.1177/0309133316633570.
- Chaouch, N., M. Temimi, S. Hagen, J. Weishampel, S. Medeiros, and R. Khanbilvardi (2012), A synergetic use of satellite imagery from SAR and optical sensors to improve coastal flood mapping in the Gulf of Mexico, *Hydrol. Processes*, 26 (11), 1617–1628; doi:10.1002/hyp.8268.
- Chini, M., A. Piscini, F. Cinti, S. Amici, R. Nappi, and P. Demartini (2013), The 2011 Tohoku (Japan) tsunami inundation and liquefaction investigated through optical, thermal, and SAR data, *IEEE Geoscience and Remote Sensing Letters*, 10 (2), 347–351; doi:10.1109/LGRS.2012.2205661.
- Chini, M., C. Bignami, S. Stramondo, and N. Pierdicca (2008), Uplift and subsidence due to the 26 December 2004 Indonesian earthquake detected by SAR data, *Int. J. Remote Sens.*, 29 (13), 3891–3910; doi:10.1080/01431160701871112.
- Chini, M., L. Pulvirenti, and N. Pierdicca (2012), Analysis and interpretation of the COSMO-SkyMed observations of the 2011 Japan tsunami, *IEEE Geoscience and Remote Sensing Letters*, 9 (3), 467–471; doi:10.1109/LGRS.2011.2182495.
- Chini, M., M. Albano, M. Saroli, L. Pulvirenti, M. Moro, C. Bignami, E. Falcucci, et al. (2015), Coseismic liquefaction phenomenon analysis by COSMO-SkyMed: 2012 Emilia (Italy) earthquake, *Int. J. App. Earth Obs. Geoinf.*, 39, 65–78; doi:10.1016/j.jag.2015.02.008.
- Chini, M., S. Member, R. Hostache, L. Giustarini, and P. Matgen (2017), A hierarchical split-based approach for parametric thresholding of SAR images: Flood inundation as a test case, *IEEE Trans. Geosci. Remote Sens.*, 1–14.
- Cohen, J., H. Riihimäki, J. Pulliainen, J. Lemmetyinen, and J. Heilimo (2016), Implications of boreal forest stand characteristics for X-band SAR flood mapping accuracy, *Remote Sens. Environ.*, 186, 47–63; doi:10.1016/j.rse.2016.08.016.
- Cossu, R., E. Schoepfer, P. Bally, and L. Fusco (2009), Near real-time SAR-based processing to support flood monitoring, *J. Real-Time Image Pro.*, 4 (3), 205–318; doi:10.1007/s11554-009-0114-4.
- De Grandi, G. F., P. Mayaux, J. P. Malingreau, A. Rosenqvist, S. Saatchi, and M. Simard (2000), New perspectives on global ecosystems from wide-area radar mosaics: Flooded forest mapping in the tropics, *Int. J. Remote Sens.*, 21 (6–7), 1235–1249; doi:10.1080/014311600210155.
- Di Baldassarre, G., G. Schumann, and P. Bates (2009), A technique for the calibration of hydraulic models using uncertain satellite observations of flood extent, *J. Hydrol.*, 367 (3–4), 276–282; doi:10.1016/j.jhydrol.2009.01.020.
- Di Baldassarre, G., G. Schumann, L. Brandimarte, and P. Bates (2011), Timely low resolution SAR imagery to support floodplain modelling: A case study review, *Surv. Geophys.*, 32, 255–269; doi:10.1007/s10712-011-9111-9.
- Di Baldassarre, G., G. Schumann, P. Bates, J. Freer, and K. Beven (2010), Flood-plain mapping: A critical discussion of deterministic and probabilistic approaches, *Hydrol. Sci. J.*, 55 (3), 364–376; doi:10.1080/02626661003683389.
- Fohringer, J., D. Dransch, H. Kreibich, and K. Schroter (2015), Social media as an information source for rapid flood inundation mapping, *Nat. Hazards Earth Syst. Sci.*, 15 (12), 2725–2738; doi:10.5194/nhess-15-2725-2015.
- Frappart, F., S. Calmant, M. Cauhope, F. Seyler, and A. Cazenave (2006), Preliminary results of ENVISAT RA-2-derived water levels validation over the Amazon basin, *Remote Sens. Environ.*, 100 (2), 252–264; doi:10.1016/j.rse.2005.10.027.
- García-Pintado, J., D. Mason, and S. Dance (2014), Moderation of ensemble covariances for data assimilation of satellite-based water level observations into flood modelling, 16 (November 2012), 11618.
- García-Pintado, J., J. Neal, D. Mason, S. Dance, and P. Bates (2013), Scheduling satellite-based SAR acquisition for

- sequential assimilation of water level observations into flood modelling, *J. Hydrol.*, 495 (July), 252–266; doi:10.1016/j.jhydrol.2013.03.050.
- Giustarini, L., H. Vernieuwe, J. Verwaeren, M. Chini, R. Hostache, P. Matgen, N. Verhoest, and B. de Baets (2015a), Accounting for image uncertainty in SAR-based flood mapping, *Int. J. App. Earth Obs. Geoinf.*, 34 (1), 70–77; doi:10.1016/j.jag.2014.06.017.
- Giustarini, L., M. Chini, R. Hostache, F. Pappenberger, and P. Matgen (2015b), Flood hazard mapping combining hydrodynamic modeling and multi annual remote sensing data, *Remote Sens.*, 7 (10), 14200–14226; doi:10.3390/rs71014200.
- Giustarini, L., R. Hostache, D. Kavetski, M. Chini, C. Giovanni, S. Schlaffer, and P. Matgen (2016), Probabilistic flood mapping using synthetic aperture radar data, *IEEE Trans. Geosci. Remote Sens.*, 54 (12), 6958–6969.
- Giustarini, L., R. Hostache, P. Matgen, G. Schumann, P. Bates, and D. Mason (2013), A change detection approach to flood mapping in urban areas using TerraSAR-X, *IEEE Trans. Geosci. Remote Sens.*, 51 (4), 2417–2430; doi:10.1109/TGRS.2012.2210901.
- Gobeyn, S., A. Van Wesemael, J. Neal, H. Lievens, K. Van Eerdenbrugh, N. De Vleeschouwer, H. Vernieuwe, et al. (2017), Impact of the timing of a SAR image acquisition on the calibration of a flood inundation model, *Adv. Water Resour.*, 100, 126–138; doi:10.1016/j.advwatres.2016.12.005.
- Gobeyn, S., J. Neill, H. Lievens, K. Van Eerdenbrugh, and N. De Vleeschouwer (2015), Impact of the SAR acquisition timing on the calibration of a flood inundation model, 17, 3822.
- Grimaldi, S., Y. Li, V. Pauwels, and J. Walker (2016), Remote sensing-derived water extent and level to constrain hydraulic flood forecasting models: Opportunities and challenges, *Surv. Geophys.*, 37 (5), 977–1034; doi:10.1007/s10712-016-9378-y.
- Gupta, H., S. Sorooshian, and P. Yapo (1998), Toward improved calibration of hydrologic models: Multiple and noncommensurable measures of information, *Water Resour. Res.*, 34 (4), 751–763.
- Hess, L., J. Melack, and D. Simonett (1990), Radar detection of flooding beneath the forest canopy: A review, *Int. J. Remote Sens.*, 11 (7), 1313–1325; doi:10.1080/01431169008955095.
- Horritt, M. S. (1999), A statistical active contour model for SAR image segmentation, *Image and Vision Computing*, 17 (3–4), 213–224; doi:10.1016/S0262-8856(98)00101-2.
- Horritt, M. S. (2000), Calibration of a Two-dimensional finite element flood flow model using satellite radar imagery, *Water Resour. Res.*, 36 (11), 3279–3291.
- Horritt, M. S., and P. Bates (2002), Evaluation of 1D and 2D numerical models for predicting river flood inundation, *J. Hydrol.*, 268, 87–99.
- Horritt, M. S., D. C. Mason, and A. J. Luckman (2001), Flood boundary delineation from synthetic aperture radar imagery using a statistical active contour model, *Int. J. Remote Sens.*, 22 (13), 2489–2507; doi:10.1080/01431160116902.
- Hostache, R., G. Schumann, P. Matgen, C. Puech, L. Hoffmann, and L. Pfister (2006), 3D flood information from SAR as a mean for reducing uncertainties in flood inundation modelling, in *XXX ISPRS Congress, Commission VII, 3D Flood Information from SAR as a Means for Reducing Uncertainties in Flood Inundation Modelling*, 217–222.
- Hostache, R., P. Matgen, and W. Wagner (2012), Change detection approaches for flood extent mapping: How to select the most adequate reference image from online archives?, *Int. J. App. Earth Obs. Geoinf.*, 19 (1), 205–213; doi:10.1016/j.jag.2012.05.003.
- Hostache, R., P. Matgen, G. Schumann, C. Puech, L. Hoffmann, and L. Pfister (2009), Water level estimation and reduction of hydraulic model calibration uncertainties using satellite SAR images of floods, *IEEE Trans. Geosci. Remote Sens.*, February, 1–10.
- Hostache, R., X. Lai, J. Monnier, and C. Puech (2010), Assimilation of spatially distributed water levels into a shallow-water flood model, Part II: Use of a remote sensing image of Mosel River, *J. Hydrol.*, 390 (3–4), 257–268; doi:10.1016/j.jhydrol.2010.07.003.
- Jain, S., R. D. Singh, M. K. Jain, and A. K. Lohani (2005), Delineation of flood-prone areas using remote sensing techniques, *Water Resour. Man.*, 19 (4), 333–347; doi:10.1007/s11269-005-3281-5.
- Kropatsch, W., and D. Strobl (1990), The Generation of SAR layover and shadow maps from digital elevation models, *IEEE Trans. Geosci. Remote Sens.*, 28 (1), 98–107; doi:10.1109/36.45752.
- Lai, X., and J. Monnier (2009), Assimilation of spatially distributed water levels into a shallow-water flood model, Part I: Mathematical method and test case, *J. Hydrol.*, 377 (1–2), 1–11; doi:10.1016/j.jhydrol.2009.07.058.
- Li, L., Y. Chen, X. Yu, R. Liu, and C. Huang (2015), Subpixel flood inundation mapping from multispectral remotely sensed images based on discrete particle swarm optimization, *ISPRS J. Photo. Rem. Sens.*, 101, 10–21; doi:10.1016/j.isprsjprs.2014.11.006.
- Lillesand, T. M., et al. (2004), *Remote Sensing and Image Interpretation*, 5th ed., John Wiley & Sons, New York.
- Martinis, S., and C. Rieke (2015), Backscatter analysis using multi-temporal and multi-frequency SAR data in the context of flood mapping at River Saale, *Germany Rem. Sens.*, 7 (6), 7732–7752; doi:10.3390/rs70607732.
- Martinis, S., A. Twele, and S. Voigt (2009), Towards operational near real-time flood detection using a split-based automatic thresholding procedure on high resolution TerraSAR-X data, *Nat. Hazards Earth Syst. Sci.*, 9 (2), 303–314; doi:10.5194/nhess-9-303-2009.
- Martinis, S., A. Twele, and S. Voigt (2011), Unsupervised extraction of flood-induced backscatter changes in SAR data using Markov image modeling on irregular graphs, *IEEE Trans. Geosci. Rem. Sens.*, 49 (1 PART 1), 251–263; doi:10.1109/TGRS.2010.2052816.
- Martinis, S., C. Kuenzer, A. Wendleder, J. Huth, A. Twele, A. Roth, and S. Dech (2015a), Comparing four operational SAR-based water and flood detection approaches, *Int. J. Rem. Sens.*, 36 (13), 3519–3543; doi:10.1080/01431161.2015.1060647.
- Martinis, S., C. Kuenzer, and A. Twele (2015b), Flood studies using synthetic aperture radar data, *Rem. Sens. Water Resour. Disas. Urb. Stud.*, 145–173; doi:10.1201/b19321-10.
- Martinis, S., J. Kersten, and A. Twele (2015c), A fully automated TerraSAR-X based flood service, *ISPRS J. Photo. Rem. Sens.*, 104, 203–212; doi:10.1016/j.isprsjprs.2014.07.014.

- Mason, D., and L. Davenport (1996), Accurate and efficient determination of the shoreline in ERS-1 SAR images, *IEEE Trans. Geosci. Rem. Sens.*, 34 (5), 1243–1253; doi:10.1109/36.536540.
- Mason, D., J. Garcia-Pintado, H. Cloke, and S. Dance (2015), The potential of flood forecasting using a variable-resolution global digital terrain model and flood extents from synthetic aperture radar images, *Front. Earth Sci.*, 3 (Aug), 1–14; doi:10.3389/feart.2015.00043.
- Mason, D., M. S. Horritt, J. Dall'Amico, T. Scott, and P. Bates (2007), Improving river flood extent delineation from synthetic aperture radar using airborne laser altimetry, *IEEE Trans. Geosci. Rem. Sens.*, 45 (12), 3932–3943; doi:10.1109/TGRS.2007.901032.
- Mason, D. C., G. J.-P. Schumann, J. C. Neal, J. Garcia-Pintado, and P. D. Bates (2012a), Automatic near real-time selection of flood water levels from high resolution synthetic aperture radar images for assimilation into hydraulic models: A case study, *Rem. Sens. Environ.*, 124, 705–716; doi:10.1016/j.rse.2012.06.017.
- Mason, D. C., I. Davenport, J. Neal, G. Schumann, and P. Bates (2012b), Near real-time flood detection in urban and rural areas using high-resolution synthetic aperture radar images, *IEEE Trans. Geosci. Rem. Sens.*, 50 (8), 3041–3052; doi:10.1109/TGRS.2011.2178030.
- Mason, D. C., R. Speck, B. Devereux, G. J. P. Schumann, J. C. Neal, and P. D. Bates (2010), Flood detection in urban areas using TerraSAR-X, *IEEE Trans. Geosci. Rem. Sens.*, 48 (2), 882–894; doi:10.1109/tgrs.2009.2029236.
- Matgen, P., J.-B. Henry, F. Pappenberger, P. de Fraipont, L. Hoffmann, and L. Pfister (2004), Uncertainty in calibrating flood propagation models with flood boundaries derived from SAR imagery, in *XX ISPRS Congress, Commission VII, Uncertainty in Calibrating Flood Propagation Models with Flood Boundaries Derived from SAR Imagery*.
- Matgen, P., L. Giustarini, M. Chini, R. Hostache, M. Wood, and S. Schlaffer (2016), Creating a water depth map from SAR flood extent and topography data, *International Geoscience and Remote Sensing Symposium (IGARSS)*, 7635–7638; doi:10.1109/IGARSS.2016.7730991.
- Matgen, P., M. Montanari, R. Hostache, L. Pfister, L. Hoffmann, D. Plaza, V. R. N. Pauwels, G. J. M. De Lannoy, R. De Keyser, and H. H. G. Savenije (2010), Towards the sequential assimilation of SAR-derived water stages into hydraulic models using the particle filter: Proof of concept, *Hydrol. Earth Syst. Sci.*, 14 (9), 1773–1785; doi:10.5194/hess-14-1773-2010.
- Matgen, P., R. Hostache, G. Schumann, L. Pfister, L. Hoffmann, and H. H. G. Savenije (2011), Towards an automated SAR-based flood monitoring system: Lessons learned from two case studies, *Phys. Chem. Earth*, 36 (7–8), 241–252; doi:10.1016/j.pce.2010.12.009.
- Nico, G., M. Pappalepore, G. Pasquariello, A. Refice, and S. Samarelli (2000), Comparison of SAR amplitude vs. coherence flood detection methods: A GIS application, *Int. J. Rem. Sens.*, 21 (8), 1619–1631; doi:10.1080/014311600209931.
- Ogilvie, A., G. Belaud, C. Delenne, J. Bailly, J. Bader, A. Oleksiak, L. Ferry, and D. Martin (2015), Decadal monitoring of the Niger inner delta flood dynamics using MODIS optical data, *J. Hydrol.*, 523, 368–383; doi:10.1016/j.jhydrol.2015.01.036.
- O'Grady, D., M. Leblanc, and A. Bass (2014), The use of radar satellite data from multiple incidence angles improves surface water mapping, *Rem. Sens. Environ.*, 140, 652–664; doi:10.1016/j.rse.2013.10.006.
- O'Grady, D., M. Leblanc, and D. Gillieson (2013), Relationship of local incidence angle with satellite radar backscatter for different surface conditions, *Int. J. App. Earth Obs. Geoinf.* 24 (1), 42–53; doi:10.1016/j.jag.2013.02.005.
- Ordoyne, C., and M. Friedl (2008), Using MODIS data to characterize seasonal inundation patterns in the Florida everglades, *Rem. Sens. Environ.*, 112, 4107–4119; doi:10.1016/j.rse.2007.08.027.
- Otsu, N. (1979), A threshold selection method from gray-level histograms, *IEEE Trans. Syst. Man Cyber.*, 9 (1), 62–66; doi:10.1109/TSMC.1979.4310076.
- Panegrossi, G., R. Ferretti, L. Pulvirenti, and N. Pierdicca (2011), Impact of ASAR soil moisture data on the MM5 precipitation forecast for the Tanaro flood event of April 2009, *Nat. Haz. Earth Syst. Sci.*, 11 (12), 3135–3149; doi:10.5194/nhess-11-3135-2011.
- Pappenberger, F., K. Frodsham, K. Beven, R. Romanovicz, and P. Matgen (2007), Fuzzy set approach to calibrating distributed flood inundation models using remote sensing observations, *Hydrol. Earth Syst. Sci.*, 11 (2), 739–752; doi:10.5194/hess-11-739-2007.
- Pierdicca, N., L. Pulvirenti, G. Boni, G. Squicciarino, and M. Chini (2017), Mapping flooded vegetation using COSMO-SkyMed: Comparison with polarimetric and optical data over rice fields, *IEEE Journal of Selected Topics in Applied Earth Observations and Remote Sensing*, 10 (6), 1–13; doi:10.1109/JSTARS.2017.2711960.
- Pierdicca, N., L. Pulvirenti, M. Chini, G. Boni, G. Squicciarino, and L. Candela (2014), Flood mapping by SAR: Possible approaches to mitigate errors due to ambiguous radar signatures. *International Geoscience and Remote Sensing Symposium (IGARSS)*, 3850–3853; doi:10.1109/IGARSS.2014.6947324.
- Pierdicca, N., L. Pulvirenti, M. Chini, L. Guerriero, and L. Candela (2013), Observing floods from space: Experience gained from COSMO-SkyMed observations, *Acta Astronaut.*, 84, 122–133; doi:10.1016/j.actaastro.2012.10.034.
- Pierdicca, N., M. Chini, L. Pulvirenti, and F. Macina (2008), Integrating physical and topographic information into a fuzzy scheme to map flooded area by SAR, *Sensors*, 8 (7), 4151–4164; doi:10.3390/s8074151.
- Plank, S., M. Jüssi, S. Martinis, and A. Twele (2017), Mapping of flooded vegetation by means of Polarimetric Sentinel-1 and ALOS-2/PALSAR-2 imagery, *Int. J. Rem. Sens.*, 38 (13), 3831–3850; doi:10.1080/01431161.2017.1306143.
- Policelli, F., D. Slayback, B. Brakenridge, J. Nigro, A. Hubbard, B. Zaitchik, M. Carroll, and H. Jung (2017), The NASA global flood mapping system, in *Remote Sensing of Hydrological Extremes, The NASA Global Flood Mapping System*, edited by R. Escobar C, J. D. Restrepo, G. R. Brakenridge, and A. J. Kettner, 47–63; doi:10.1007/978-3-319-43744-6.
- Pradhan, B., M. Tehrany, and M. Jebur (2016), A new semiautomated detection mapping of flood extent from TerraSAR-X

- satellite image using rule-based classification and Taguchi optimization techniques, *IEEE Trans. Geosci. Rem. Sens.*; doi:10.1109/TGRS.2016.2539957.
- Pradhan, B., U. Hagemann, M. Tehrany, and N. Prechtel (2014), An easy to use arcmap based texture analysis program for extraction of flooded areas from TerraSAR-X satellite image. *Comput. Geosci.*, 63 (Feb.), 34–43; doi:10.1016/j.cageo.2013.10.011.
- Pulvirenti, L., F. Marzano, N. Pierdicca, S. Mori, and M. Chini (2014a), Discrimination of water surfaces, heavy rainfall, and wet snow using COSMO-SkyMed observations of severe weather events, *IEEE Trans. Geosci. Rem. Sens.*, 52 (2), 858–869; doi:10.1109/TGRS.2013.2244606.
- Pulvirenti, L., M. Chini, F. Marzano, N. Pierdicca, S. Mori, L. Guerriero, G. Boni, and L. Candela (2012), Detection of floods and heavy rain using Cosmo-SkyMed data: The event in northwestern Italy of November 2011, *International Geoscience and Remote Sensing Symposium (IGARSS)*, 3026–3029; doi:10.1109/IGARSS.2012.6350788.
- Pulvirenti, L., M. Chini, N. Pierdicca, and G. Boni (2015), Use of SAR data for detecting floodwater in urban and agricultural areas: The role of the interferometric coherence, *IEEE Trans. Geosci. Rem. Sens.*, 54 (3), 1532–1544; doi:10.1109/TGRS.2015.2482001.
- Pulvirenti, L., M. Chini, N. Pierdicca, L. Guerriero, and P. Ferrazzoli (2011a), Flood monitoring using multi-temporal COSMO-SkyMed data: Image segmentation and signature interpretation, *Rem. Sens. Environ.*, 115 (4), 990–1002; doi:10.1016/j.rse.2010.12.002.
- Pulvirenti, L., N. Pierdicca, G. Boni, M. Fiorini, and R. Rudari (2014b), Flood damage assessment through multitemporal COSMO-SkyMed data and hydrodynamic models: The Albania 2010 case study, *IEEE Journal of Selected Topics in Applied Earth Observations and Remote Sensing*, 7 (7): 2848–2855; doi:10.1109/JSTARS.2014.2328012.
- Pulvirenti, L., N. Pierdicca, M. Chini, and L. Guerriero (2011b), An algorithm for operational flood mapping from synthetic aperture radar (SAR) data using fuzzy logic, *Nat. Haz. Earth Syst. Sci.*, 11 (2), 529–540; doi:10.5194/nhess-11-529-2011.
- Pulvirenti, L., N. Pierdicca, M. Chini, and L. Guerriero (2013), Monitoring flood evolution in vegetated areas using Cosmo-SkyMed data: The Tuscany 2009 case study, *IEEE Journal of Selected Topics in Applied Earth Observations and Remote Sensing*, 6 (4), 1807–1816; doi:10.1109/JSTARS.2012.2219509.
- Rees, W. G. (2013), *Physical Principles of Remote Sensing*, Cambridge University Press.
- Refice, A., D. Capolongo, G. Pasquariello, A. Daaddabbo, F. Bovenga, R. Nutricato, F. P. Lovergine, and L. Pietranera (2014), SAR and InSAR for flood monitoring: examples with COSMO-SkyMed data, *IEEE Journal of Selected Topics in Applied Earth Observations and Remote Sensing*, 7 (7), 2711–2722; doi:10.1109/JSTARS.2014.2305165.
- Richards, J. A., P. W. Woodgate, and A. K. Skidmore (1987), An explanation of enhanced radar backscattering from flooded forests, *Int. J. Rem. Sens.*, 8 (7), 1093–1100; doi:10.1080/01431168708954756.
- Sala, J., A. Lopez, L. Romero, and F. Koudogbo (2016), A Sentinel-1 flood map generation QGIS plugin, 18, 14693.
- Schlaffer, S., M. Chini, D. Dettmering, and W. Wagner (2016), Mapping wetlands in Zambia using seasonal backscatter signatures derived from ENVISAT ASAR time series, *Rem. Sens.*, 8 (5), 1–24; doi:10.3390/rs8050402.
- Schlaffer, S., M. Chini, L. Giustarini, and P. Matgen (2017), Probabilistic mapping of flood-induced backscatter changes in SAR time series, *Int. J. App. Earth Obs. Geoinf.*, 56, 77–87; doi:10.1016/j.jag.2016.12.003.
- Schlaffer, S., P. Matgen, M. Hollaus, and W. Wagner (2015), Flood detection from multi-temporal SAR data using harmonic analysis and change detection, *Int. J. App. Earth Obs. Geoinf.* 38, 15–24; doi:10.1016/j.jag.2014.12.001.
- Schumann, G., and D. Moller (2015), Microwave remote sensing of flood inundation, *Phys. Chem. Earth*, 83–84, 84–95; doi:10.1016/j.pce.2015.05.002.
- Schumann, G., and G. Di Baldassarre (2010), The direct use of radar satellites for event-specific flood risk mapping, *Rem. Sens. Lett.*, 1 (2), 75–84; doi:10.1080/01431160903486685.
- Schumann, G., F. Pappenberger, and P. Matgen (2008a), Estimating uncertainty associated with water stages from a single SAR image, *Adv. Water Resour.*, 31 (8), 1038–1047; doi:10.1016/j.adwatres.2008.04.008.
- Schumann, G., G. Di Baldassarre, and P. Bates (2009), The utility of spaceborne radar to render flood inundation maps based on multialgorithm ensembles, *IEEE Trans. Geosci. Rem. Sens.*, 47 (8), 2801–2807; doi:10.1109/TGRS.2009.2017937.
- Schumann, G., M. Cutler, A. Black, P. Matgen, L. Pfister, L. Hoffmann, and F. Pappenberger (2008b), Evaluating uncertain flood inundation predictions with uncertain remotely sensed water stages, *Int. J. River Basin Man.*, 5124 (Nov. 2014), 37–41; doi:10.1080/15715124.2008.9635347.
- Schumann, G., P. Matgen, L. Hoffmann, R. Hostache, F. Pappenberger, and L. Pfister (2007a), Deriving distributed roughness values from satellite radar data for flood inundation modelling, *J. Hydrol.*, 344 (1–2), 96–111; doi:10.1016/j.jhydrol.2007.06.024.
- Schumann, G., R. Hostache, C. Puech, L. Hoffmann, P. Matgen, F. Pappenberger, and L. Pfister (2007b), High-resolution 3-D flood information from radar imagery for flood hazard management, *IEEE Trans. Geosci. Rem. Sens.*, 45 (6), 1715–1725; doi:10.1109/TGRS.2006.888103.
- Schumann, G., S. Frye, G. Wells, R. Adler, R. Brakenridge, J. Bolten, J. Murray, et al (2016), Unlocking the full potential of earth observation during the 2015 Texas flood disaster. *Water Resour. Res.* 52 (1), 3288–3293; doi:10.1002/2015WR017126. Received.
- Schumann, G. J. P., and A. Domeneghetti (2016), Exploiting the proliferation of current and future satellite observations of rivers, *Hydrol. Processes*, 30 (16), 2891–2896; doi:10.1002/hyp.10825.
- Schumann, G. J. P., J. C. Neal, D. C. Mason, and P. D. Bates (2011), The accuracy of sequential aerial photography and SAR data for observing urban flood dynamics, a case study of the UK summer 2007 floods, *Rem. Sens. Environ.*, 115 (10), 2536–2546; doi:10.1016/j.rse.2011.04.039.
- Stephens, E. M. M., P. D. D. Bates, J. E. E. Freer, and D. C. C. Mason (2012), The impact of uncertainty in satellite data on

- the assessment of flood inundation models, *J. Hydrol.* 414–415 (Jan.), 162–73; doi:10.1016/j.jhydrol.2011.10.040.
- Thiele, A., E. Cadario, K. Schulz, and U. Thoennessen (2007), Model-based building recognition from multi-aspect inSAR data in urban areas, *IEEE Trans. Geosci. Rem. Sens.*, 45 (11), 3583–3593.
- Townsend, P. A. (2001), Mapping seasonal flooding in forested wetlands using multi-temporal radarsat SAR, *Photo. Eng. Rem. Sens.*, 67 (7). https://www.researchgate.net/publication/246763152_Mapping_seasonal_flooding_in_forested_wetlands_using_multi-temporal_Radarsat_SAR.
- Twele, A., W. Cao, S. Plank, and S. Martinis (2016), Sentinel-1-based flood mapping: a fully automated processing chain, *Int. J. Rem. Sens.*, 37 (13), 2990–3004; doi:10.1080/01431161.2016.1192304.
- Ulaby, F., D. Long, W. Blackwell, C. Elachi, A. Fung, C. Ruf, K. Sarabandi, H. A. Zebker, and J. Van Zyl (2014), *Microwave Radar and Radiometric Remote Sensing*, Vol. 4, No. 5, University of Michigan Press, Ann Arbor.
- Voormansik, K., J. Praks, O. Antropov, J. Jagomagi, and K. Zalite (2014), Flood mapping with TerraSAR-X in forested regions in Estonia, *IEEE Journal of Selected Topics in Applied Earth Observations and Remote Sensing*, 7 (2), 562–577; doi:10.1109/JSTARS.2013.2283340.
- Wdowinski, S., S. W. Kim, F. Amelung, T. Dixon, F. Miralles-Wilhelm, and R. Sonenshein (2008), Space-based detection of wetlands' surface water level changes from L-Band SAR interferometry, *Rem. Sens. Environ.*, 112 (3), 681–696; doi:10.1016/j.rse.2007.06.008.
- Westerhoff, R. S., M. Kleuskens, H. C. Winsemius, H. J. Huizinga, G. R. Brakenridge, and C. Bishop (2013), Automated global water mapping based on wide-swath orbital synthetic-aperture radar, *Hydrol. Earth Syst. Sci.*, 17 (2), 651–663; doi:10.5194/hess-17-651-2013.
- Weydahl, D. J. (1996), Flood monitoring in Norway using ERS-1 SAR images, *International Geoscience and Remote Sensing Symposium 1 (IGARSS)*, 151–153; doi:10.1109/IGARSS.1996.516274.
- Wood, M., R. Hostache, J. Neal, T. Wagener, L. Giustarini, M. Chini, G. Corato, P. Matgen, and P. Bates (2016), Calibration of channel depth and friction parameters in the LISFLOOD-FP hydraulic model using medium-resolution SAR data and identifiability techniques, *Hydrol. Earth Syst. Sci.*, 20 (12), 4983–4997; doi:10.5194/hess-20-4983-2016.
- Woodhouse, I. H. (2005), *Introduction to Microwave Remote Sensing*, CRC Press.
- Zalite, K., K. Voormansik, A. Olesk, M. Noorma, and A. Reinart (2014), Effects of inundated vegetation on X-Band HH-VV backscatter and phase difference, *IEEE Journal of Selected Topics in Applied Earth Observations and Remote Sensing*, 7(4), 1402–1406; doi:10.1109/JSTARS.2013.2279552.
- Zebker, H. A., and J. Villasenor (1992), Decorrelation in interferometric radar echoes, *IEEE Trans. Geosci. Rem. Sens.*, 30 (5), 950–959; doi:10.1109/36.175330.